Garcia-Gonzalez, D., Garzon-Hernandez, S. & Arias, A. (2018). A new constitutive model for polymeric matrices: Application to biomedical materials. *Composites Part B: Engineering*, vol. 139, pp. 117-129.

DOI: 10.1016/j.compositesb.2017.11.045

A new constitutive model for polymeric matrices: Application to biomedical materials

D. Garcia-Gonzalez[a,b], S. Garzon-Hernandez[b], A. Arias*[b]

[a] Department of Engineering Science, University of Oxford, Parks Road, Oxford OX1 3PJ, UK
[b] Department of Continuum Mechanics and Structural Analysis, University Carlos III of Madrid, Avda. de la Universidad 30, 28911 Leganés, Madrid, Spain

***Corresponding author: aariash@ing.uc3m.es (Angel Arias)**

Abstract: Semi-crystalline polymeric composites are increasingly used as bearing material in the biomedical sector, mainly because of their specific mechanical properties and the new advances in 3D printing technologies that allows for customised devices. Among these applications, total or partial prostheses for surgical purposes must consider the influence of temperature and loading rate. This paper proposes a new constitutive model for semi-crystalline polymers, commonly used as matrix material in a wide variety of biomedical composites, that enables reliable predictions under a wide range of loading conditions. The most recent models present limitations to predict the non-linear behaviour of the polymer when it is exposed to large deformations at high strain rates. The proposed model takes into account characteristic behaviours of injected and 3D printed thermoplastic polymers such as material hardening due to strain rate sensitivity, thermal softening, thermal expansion and combines viscoelastic and viscoplastic responses. These viscous-behaviours are relevant for biomedical applications where temperature evolution is expected during the deformation process due to heat generation induced by inelastic dissipation, being essential the thermo-mechanical coupling consideration. The constitutive model is formulated for finite deformations within a thermodynamically consistent framework. Additionally, the model is implemented in a finite element code and its parameters are identified for two biomedical polymers: ultra-high-molecular-weight-polyethylene (UHMWPE) and high density polyethylene (HDPE). Finally, the influence of viscous behaviours on dynamic deformation of semi-crystalline polymeric matrices is analysed. This constitutive model predicts the mechanical behaviour of semi-crystalline polymeric matrices for a wide range of strain rate and temperature conditions, allowing for the optimisation of new composite materials potentially used as effective joint replacement prostheses.

Keywords: Biomedical materials; Polymer–matrix composites (PMCs); Constitutive model; UHMWPE composites.

1. Introduction

Semi-crystalline polymers and their composites are currently used in a wide range of applications that are subjected to dynamic loading [1-4]. In several applications, the dynamic deformation of these polymers is an essential consideration, such as in the biomedical, the aeronautical and the automotive industries [5]. Among the materials employed as matrix in a wide variety of composites, these polymers stand out due to their wear resistance, biocompatibility and good mechanical properties [6-8]. In the biomedical sector, injection moulded and 3D printed polymers are used as bearing material for prostheses [9-12], highlighting their use in hip and knee joints [13]. In such applications, the pure polymeric material still presents mechanical limitations in terms of severe material degradation, Fig.1, and damage arising from its low hardness, its

relatively low stiffness, as well as high creep rate under load [14,15]. In order to enhance its mechanical properties, a wide range of fillers are used: carbon fibres, hard particles, hydroxyapatite, boron carbide and graphene oxide nanoparticles [2,16,17]. The advance in the 3D printed polymeric composites field requires, then, the proper understanding of the mechanical behaviour of matrix materials. In this regard, semi-crystalline polymers behave in a complex manner that presents a strong non-linearity and depends on many factors such as strain rate [18], temperature [19], stress state [20], large deformations and plastic flow [21]. Therefore, the proper understanding of the polymeric matrix is essential for the study of the mechanical response of the composite. To this end, constitutive models for reliable predictions of the mechanical behaviour of such materials must account for strain rate, temperature and stress state dependences combining both viscoelastic and viscoplastic behaviours.

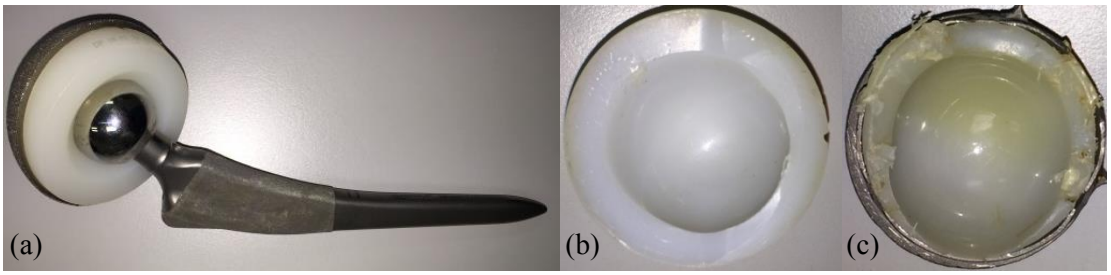

Fig. 1. (a) Real polyethylene-metal hip prosthetic. (b)-(c) Polyethylene acetabular cup removed from patients due to excessive material erosion. Materials provided by Dra. I. Gómez Arrayás (Hospital Ruber Internacional of Madrid).

Moreover, fibre reinforced semi-crystalline composites are also used in structural components for applications that require excellent impact performance [22]. In this regard, when semi-crystalline polymers are used in aeronautical -for example, as bulk space filters- and automotive applications -for example, as vehicle crashworthiness structural components-, other effects must be also accounted for faithfully describing its mechanical behaviour. The exposure of this polymer to high strain rates leads to variations in its response [23]. In this sense, there is a positive dependence of elastic modulus and yield stress on strain rate [18,24]. In addition, there is a strong coupling between the mechanical and thermal behaviours of the polymer which becomes more relevant at high strain rates [12,19,25]. When the polymer exhibits large deformations, there is a heat generation due to inelastic-viscous dissipation that induces an increase in material temperature leading to thermal softening. These thermal effects have a strong influence on the mechanical behaviour of semi-crystalline polymers at high strain rates and should be considered by constitutive models for providing reliable predictions of their behaviour. Under dynamic conditions, the understanding of the composite matrix becomes essential when strain rate and temperature play an important role in its behaviour, resulting in variations of the composite mechanical response [25-29].

Many constitutive approaches have been developed for modelling the mechanical behaviour of semi-crystalline polymers and, particularly, of several types of polyethylene. The first approaches, as the work developed by Hughes [30], described the mechanical response of these polymers by classical isotropic, rate-independent plasticity using Mises yield criterion. Following this line, several authors have used constitutive models to analyse the mechanical response of ultra-high-molecular-weight-polyethylene (UHMWPE) components of hip and knee prosthesis under different loading conditions, where a Mises yield surface is associated with a flow rule followed by isotropic hardening [31-33]. However, these models cannot provide reliable predictions of the non-linear behaviour of the polymer when it is exposed to large deformations.

In addition, these models present considerable limitations when the structural component deforms at high strain rates. In order to develop more robust and reliable constitutive models for semi-crystalline polymers, some authors have proposed viscoelastic-viscoplastic rheological models combining springs and dashpots to capture the inelastic response [34,35]. These models allow for taking into account the non-linear response through the constitutive definition of the springs and the rate-dependent response through the flow rule definition of the dashpots. In this regard, Bergström et al. [36] developed a constitutive model, called hybrid model, for predicting the large strain time-dependent behaviour of UHMWPE. More recently, based on previous models [37,38], Ayoub et al. [39] presented a constitutive model for polyethylene that includes a visco-hyperelastic network resistance acting in parallel with a viscoelastic-viscoplastic intermolecular resistance, where the amorphous and crystalline phases are taken under consideration. Moreover, Garcia-Gonzalez et al. [19] proposed a constitutive model for semi-crystalline polymers formulated in finite deformations where temperature dependence is additionally taken into account.

For reliable modelling of a group of semi-crystalline polymeric matrices is necessary to take into account not only viscoplasticity but also viscoelasticity. The model developed herein considers strain rate and temperature dependences, pressure sensitivity, thermal expansion and thermo-mechanical coupling considering temperature evolution due to inelastic dissipation from viscoelastic and viscoplastic deformation. Regarding temperature dependency, this influence is incorporated for both intermolecular and network stretching resistances. The constitutive equations are formulated in finite deformations within a thermodynamically consistent framework. The constitutive framework is implemented in a VUMAT subroutine for the commercial finite element solver Abaqus/Explicit [40]. The model parameters are identified for UHMWPE and for high density polyethylene (HDPE), two widely used materials in orthopaedics applications, from experimental data reported by Brown et al. [18]. Moreover, the constitutive model is suitable for predicting the mechanical behaviour of a wide variety of polymeric matrices. The application of the model to the study of stretching tests on polymers has demonstrated the importance of taking into account viscous behaviours and thermo-mechanical coupling. This study shows how specific deformation mechanisms govern the mechanical response of polymers and can lead to global or local deformations. The model developed herein is physically motivated on the deformation mechanisms behind the mechanical behaviour of semi-crystalline polymeric matrices and is observed to faithfully describe their mechanical response under a wide range of loading conditions. The work aims at providing a proper understanding of the mechanical behaviour of polymeric matrices, allowing for the development of new composite materials, especially when dealing with dynamic applications.

2. Description of the constitutive model

Semi-crystalline polymeric matrices often exhibit complex viscous effects where both viscoelastic and viscoplastic behaviours are combined. In addition, their stress-strain response can be physically interpreted as the combination of overcoming an intermolecular resistance which is increased by the development of strain-induced crystallization; and a network resistance caused by molecular orientation. The intermolecular resistance may exhibit rate-dependency that can be described by viscoplasticity. The network resistance is commonly defined as purely elastic but it may also exhibit rate-dependency that can be potentially described by viscoelasticity. In addition, viscous contributions to the mechanical behaviour of thermoplastic polymers lead to

temperature increments due to inelastic dissipation and, consequently, induce thermal softening in the material behaviour.

Motivated on the evidence introduced above, this work proposes a constitutive model that incorporates viscous behaviours in the mechanical response of semi-crystalline thermoplastic materials. The model is based on three constitutive branches according to the rheological scheme shown in Fig. 2. Here, the intermolecular resistance (I) introduces a rate- and temperature-dependent part that is defined by a Neo-Hookean hyperelastic spring and a nonlinear viscoplastic dashpot. The network resistance (N) introduces a non-linear temperature-dependent hyperelastic part that is defined by a modified eight-chain spring. The third viscous constitutive branch introduces viscoelasticity through a non-linear hyperelastic response which depends on strain rate.

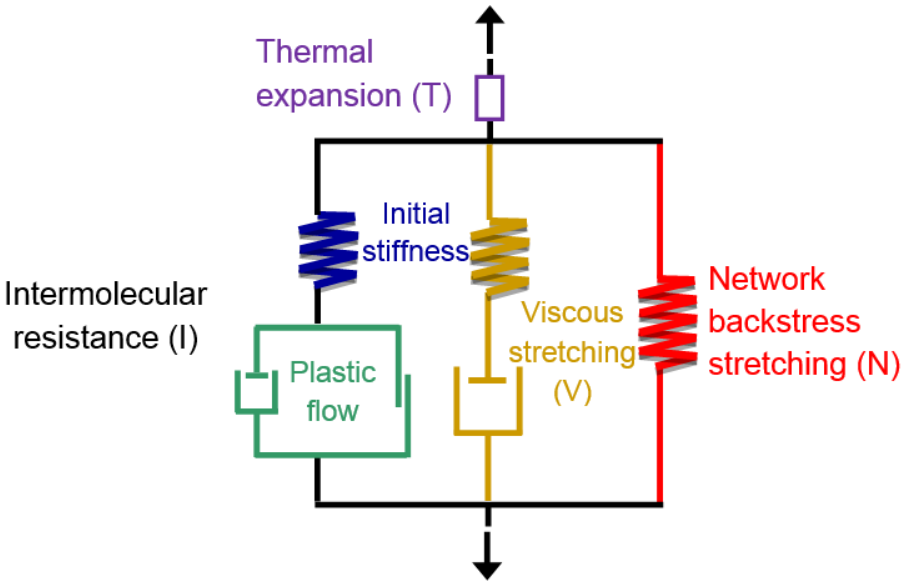

Fig. 2. Rheological scheme of the proposed constitutive model.

According to the arrangement of the rheological model elements depicted in Fig. 2, the total Cauchy stress $\boldsymbol{\sigma}$ is determined by the contribution of the intermolecular $\boldsymbol{\sigma_I}$, the network backstress $\boldsymbol{\sigma_N}$ and the viscous $\boldsymbol{\sigma_V}$ resistances:

$$\boldsymbol{\sigma} = \boldsymbol{\sigma_I} + \boldsymbol{\sigma_N} + \boldsymbol{\sigma_V} \tag{1}$$

In order to facilitate the understanding of this section, a summery with the nomenclature used along the formulation is presented in Appendix A.

2.1. Kinematics

The kinematics of the model proposed herein are based on the establishment of five spatial configurations, see Fig. 3. This kinematics goes from an initial reference configuration Ω_o to a final deformed or current configuration Ω. Three more spatial configurations are defined to allow the determination of the constitutive equations associated to each constitutive element. The first one is referred to as a dilated configuration $\overline{\Omega}$ in which only thermal deformation is accounted for; the second one is referred to as a plastic dilated relaxed configuration $\overline{\overline{\Omega}}$ in which both thermal

and plastic deformations are accounted for; and the third one is referred to as a viscous dilated relaxed configuration $\widetilde{\Omega}$ in which both thermal and viscous deformations are accounted for.

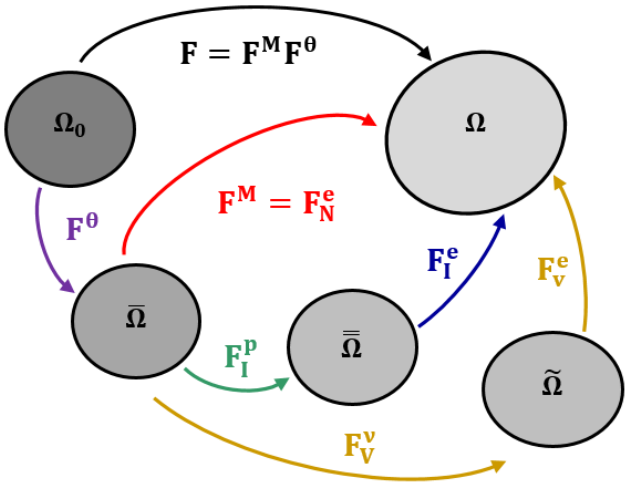

Fig. 3. Kinematics of the model showing the reference or initial configuration Ω_o, the dilated configuration $\bar{\Omega}$, the plastic dilated relaxed configuration $\bar{\bar{\Omega}}$, the viscous dilated relaxed configuration $\widetilde{\Omega}$, and the current or loaded configuration Ω.

According to the kinematics, the deformation gradient $\mathbf{F}$ is broken down into thermal, $\mathbf{F^\theta}$, and mechanical, $\mathbf{F^M}$, parts [41,42]. Thus, the total deformation gradient reads as:

$$\mathbf{F} = \mathbf{F^M F^\theta} \tag{2}$$

The mechanical part of the deformation gradient, $\mathbf{F^M}$, is equivalent for the three constitutive branches according to the rheological model. The mechanical part associated to the network resistance is defined as purely elastic, $\mathbf{F_N^e}$; the part associated to the intermolecular resistance is divided into elastic, $\mathbf{F_I^e}$, and plastic, $\mathbf{F_I^p}$, components; and the part associated to the viscoelastic resistance is divided into elastic, $\mathbf{F_V^e}$, and viscous, $\mathbf{F_V^v}$, components. Therefore, the total deformation gradient can be decomposed depending on the constitutive branch as:

$$\mathbf{F} = \mathbf{F_I^e F_I^p F^\theta} = \mathbf{F_N^e F^\theta} = \mathbf{F_V^e F_V^v F^\theta} \tag{3}$$

The velocity gradient $\mathbf{l}$, in terms of the kinematics associated with the viscous resistance elements, can be written using Eq. (3) as:

$$\mathbf{l} = \dot{\mathbf{F}}\mathbf{F}^{-1} = \mathbf{l_V^e} + \mathbf{F_V^e}\tilde{\mathbf{L}}_\mathbf{V}^\mathbf{v}\mathbf{F_V^{-e}} + \mathbf{F_V^e F_V^v}\bar{\mathbf{L}}^\mathbf{\theta}\mathbf{F_V^{-v}F_V^{-e}} \tag{4}$$

where $\mathbf{l_V^e} = \dot{\mathbf{F}}_\mathbf{V}^\mathbf{e}\mathbf{F_V^{-e}}$ is the elastic component of the velocity gradient in the current configuration and the viscous component $\tilde{\mathbf{L}}_\mathbf{V}^\mathbf{v}$ can be defined in the viscous dilated relaxed configuration $\widetilde{\Omega}$ as:

$$\tilde{\mathbf{L}}_\mathbf{V}^\mathbf{v} = \dot{\mathbf{F}}_\mathbf{V}^\mathbf{v}\mathbf{F_V^{-v}} \tag{5}$$

This velocity gradient, as well as the plastic velocity gradient of the intermolecular resistance $\bar{\bar{\mathbf{L}}}_\mathbf{I}^\mathbf{p} = \bar{\bar{\mathbf{D}}}_\mathbf{I}^\mathbf{p} + \bar{\bar{\mathbf{W}}}_\mathbf{I}^\mathbf{p}$, can be decomposed into its symmetric and skew parts by $\tilde{\mathbf{L}}_\mathbf{V}^\mathbf{v} = \tilde{\mathbf{D}}_\mathbf{V}^\mathbf{v} + \tilde{\mathbf{W}}_\mathbf{V}^\mathbf{v}$. In this work, $\widetilde{\Omega}$ and $\bar{\bar{\Omega}}$ are assumed to be invariant to the rigid body rotations of the current configuration, that is $\tilde{\mathbf{W}}_\mathbf{V}^\mathbf{v}$=$\bar{\bar{\mathbf{W}}}_\mathbf{I}^\mathbf{p}$=$\mathbf{0}$, and therefore $\tilde{\mathbf{D}}_\mathbf{V}^\mathbf{v}$=$\tilde{\mathbf{L}}_\mathbf{V}^\mathbf{v}$ and $\bar{\bar{\mathbf{D}}}_\mathbf{I}^\mathbf{p}$=$\bar{\bar{\mathbf{L}}}_\mathbf{I}^\mathbf{p}$ [43,44]. The thermal contribution is assumed

isotropic according to Bouvard et al. [45], so that $\mathbf{F^{\theta}}$ is spherical and it is possible to assume $\bar{\mathbf{W}}^{\boldsymbol{\theta}} = \mathbf{0}$.

The kinematics of the intermolecular and network resistances have been defined in agreement with standard approaches from literature [19].

2.2. Thermodynamics

This section provides the modelling assumptions made for the formulation of the Helmholtz free energy function from which the constitutive equations derive. In addition, the thermodynamic consistency is verified from the development of the Clausius-Duhem inequality expressed in the dilated configuration (this is the common configuration for the three constitutive branches).

The Helmholtz free energy function per unit volume in the dilated configuration $\bar{\Psi}$, is defined as the additive combination of the deformation resistances [46,47] as:

$$\bar{\Psi}(\mathbf{C_I^e}, \mathbf{C_V^e}, \mathbf{C_N^e}, \theta) = \bar{\Psi}^{\mathrm{I}}(\mathbf{C_I^e}, \theta) + \bar{\Psi}^{\mathrm{V}}(\mathbf{C_V^e}) + \bar{\Psi}^{\mathrm{N}}(\mathbf{C_N^e}, \theta) \tag{6}$$

where the Helmholtz free energy depends on the elastic right Cauchy-Green deformation tensors $\mathbf{C_I^e} = \mathbf{F_I^{eT}F_I^e}$, $\mathbf{C_V^e} = \mathbf{F_V^{eT}F_V^e}$ and $\mathbf{C_N^e} = \mathbf{F_N^{eT}F_N^e}$, and temperature θ.

From the definition of the Helmholtz free energy $\bar{\Psi} = \bar{e} - \theta\bar{\eta}$, the time derivative of $\bar{\Psi}$ can be calculated as:

$$\dot{\bar{\Psi}} = \frac{\partial\bar{\Psi}}{\partial\mathbf{C_I^e}} : \dot{\mathbf{C}}_\mathbf{I}^\mathbf{e} + \frac{\partial\bar{\Psi}}{\partial\mathbf{C_V^e}} : \dot{\mathbf{C}}_\mathbf{V}^\mathbf{e} + \frac{\partial\bar{\Psi}}{\partial\mathbf{C_N^e}} : \dot{\mathbf{C}}_\mathbf{N}^\mathbf{e} + \frac{\partial\bar{\Psi}}{\partial\theta}\dot{\theta} \tag{7}$$

Using these modelling assumptions for the definition of $\bar{\Psi}$, the Clausius-Duhem inequality can be obtained from the combination of the first and second thermodynamics principles following the procedure used by Garcia-Gonzalez et al. [19] as:

$$\left(\mathbf{F_I^p}\bar{\mathbf{S}}_\mathbf{I}\mathbf{F_I^{pT}} - 2\frac{\partial\bar{\Psi}}{\partial\mathbf{C_I^e}}\right) : \mathbf{F_I^{eT}d_I^eF_I^e} + \left(\mathbf{F_V^v}\bar{\mathbf{S}}_\mathbf{V}\mathbf{F_V^{vT}} - 2\frac{\partial\bar{\Psi}}{\partial\mathbf{C_V^e}}\right) : \mathbf{F_V^{eT}d_V^eF_V^e} + \left(\bar{\mathbf{S}}_\mathbf{N} - 2\frac{\partial\bar{\Psi}}{\partial\mathbf{C_N^e}}\right) : \mathbf{F_N^{eT}d_N^eF_N^e} +$$
$$\bar{\mathbf{M}}_\mathbf{I} : \bar{\mathbf{D}}^\mathbf{p} + \bar{\mathbf{M}}_\mathbf{V} : \bar{\mathbf{D}}^\mathbf{v} + \left(-\frac{\partial\bar{\Psi}}{\partial\theta} - 3f_\theta\bar{\Psi} - \bar{\eta} + f_\theta(\bar{\mathbf{M}}_\mathbf{I} + \bar{\mathbf{M}}_\mathbf{V} + \bar{\mathbf{M}}_\mathbf{N}) : \mathbf{I}\right)\dot{\theta} - \frac{1}{\theta}\bar{\mathbf{Q}}\bar{\nabla}_\mathrm{x}\theta \geq 0 \tag{8}$$

where $\bar{\mathbf{S}}_\mathbf{I}$, $\bar{\mathbf{S}}_\mathbf{N}$ and $\bar{\mathbf{S}}_\mathbf{V}$ are respectively the corresponding second Piola-Kirchhoff stress tensors of the intermolecular, network and viscous resistances expressed in the configuration $\bar{\Omega}$ as $\bar{\mathbf{S}}_\mathbf{i} = \mathrm{J}^\mathrm{M}\mathbf{F_i^{-M}}\boldsymbol{\sigma}_\mathbf{i}\mathbf{F_i^{-MT}}$ and $\bar{\mathbf{M}}_\mathbf{I}$, $\bar{\mathbf{M}}_\mathbf{N}$ and $\bar{\mathbf{M}}_\mathbf{V}$ are respectively the Mandel stress tensors of the intermolecular, network and viscous resistances in $\bar{\Omega}$ as $\bar{\mathbf{M}}_\mathbf{i} = \mathbf{F_i^{MT}F_i^M}\bar{\mathbf{S}}_\mathbf{i}$ with *i={I,N,V}*. $\mathbf{d_I^e}$, $\mathbf{d_N^e}$ and $\mathbf{d_V^e}$ are the symmetric part of the velocity gradient tensors in Ω of the intermolecular, the network and the viscous resistances; f_θ is a temperature-dependent function; $\bar{\eta}$ is the specific entropy per unit volume in $\bar{\Omega}$; and $\bar{\mathbf{Q}}$ is the heat flux per unit volume in $\bar{\Omega}$.

Using standard arguments of the Coleman and Noll method [48,49], the second Piola-Kirchhoff stress tensor associated with each constitutive branch and the specific internal entropy per unit volume that satisfy the second law of thermodynamics along arbitrary thermodynamic processes must read as:

$$\bar{\mathbf{S}}_\mathbf{I} = \mathbf{F_I^{-p}}2\frac{\partial\bar{\Psi}}{\partial\mathbf{C_I^e}}\mathbf{F_I^{-pT}} \tag{9.1}$$

$$\bar{\mathbf{S}}_\mathbf{N} = 2\frac{\partial\bar{\Psi}}{\partial\mathbf{C_N^e}} \tag{9.2}$$

$$\bar{\mathbf{S}}_{\mathbf{V}} = \mathbf{F}_{\mathbf{V}}^{-\nu} 2 \frac{\partial \bar{\Psi}}{\partial \mathbf{C}_{\mathbf{V}}^{\mathbf{e}}} \mathbf{F}_{\mathbf{V}}^{-\nu \mathbf{T}} \tag{9.3}$$

$$\bar{\eta} = -\frac{\partial \bar{\Psi}}{\partial \theta} - 3 f_\theta \bar{\Psi} + f_\theta (\bar{\mathbf{M}}_{\mathbf{I}} + \bar{\mathbf{M}}_{\mathbf{V}} + \bar{\mathbf{M}}_{\mathbf{N}}) : \mathbf{I} \tag{9.4}$$

2.3. Thermal expansion

The thermal expansion is assumed to be isotropic, being the contribution of the thermal part to the deformation gradient defined in the form:

$$\dot{\mathbf{F}}^{\boldsymbol{\theta}} = f_\theta \mathbf{F}^{\boldsymbol{\theta}} \dot{\theta} \tag{10}$$

where $\dot{\theta}$ is the time derivative of current temperature and $f_\theta = \alpha_\theta$ is the thermal expansion coefficient. The temperature evolution equation can be deduced following the methodology used by Garcia-Gonzalez et al. [19] as:

$$\begin{aligned} &\left(\bar{C} + 3 f_\theta \bar{e} - f_\theta \left(\mathbf{F}_{\mathbf{I}}^{\mathbf{pT}} \mathbf{C}_{\mathbf{I}}^{\mathbf{e}} \mathbf{F}_{\mathbf{I}}^{\mathbf{p}} : \bar{\mathbf{S}}_{\mathbf{I}} + \mathbf{C}_{\mathbf{N}}^{\mathbf{e}} : \bar{\mathbf{S}}_{\mathbf{N}} + \mathbf{F}_{\mathbf{V}}^{\nu \mathbf{T}} \mathbf{C}_{\mathbf{V}}^{\mathbf{e}} \mathbf{F}_{\mathbf{V}}^{\nu} : \bar{\mathbf{S}}_{\mathbf{V}}\right)\right) \dot{\theta} = \bar{\mathbf{M}}_{\mathbf{I}} : \bar{\mathbf{D}}^{\mathbf{p}} + + \bar{\mathbf{M}}_{\mathbf{V}} : \bar{\mathbf{D}}^{\nu} \\ &\theta \left[\frac{3}{2} f_\theta \mathbf{F}_{\mathbf{I}}^{\mathbf{p}} \bar{\mathbf{S}}_{\mathbf{I}} \mathbf{F}_{\mathbf{I}}^{\mathbf{pT}} - f_\theta \frac{\partial \left(\mathbf{F}_{\mathbf{I}}^{\mathbf{pT}} \mathbf{C}_{\mathbf{I}}^{\mathbf{e}} \mathbf{F}_{\mathbf{I}}^{\mathbf{p}} : \bar{\mathbf{S}}_{\mathbf{I}}\right)}{\partial \mathbf{C}_{\mathbf{I}}^{\mathbf{e}}} + \frac{1}{2} \frac{\partial \left(\mathbf{F}_{\mathbf{I}}^{\mathbf{p}} \bar{\mathbf{S}}_{\mathbf{I}} \mathbf{F}_{\mathbf{I}}^{\mathbf{pT}}\right)}{\partial \theta}\right] : \dot{\mathbf{C}}_{\mathbf{I}}^{\mathbf{e}} + \theta \left[\frac{3}{2} f_\theta \bar{\mathbf{S}}_{\mathbf{N}} - f_\theta \frac{\partial (\mathbf{C}_{\mathbf{N}}^{\mathbf{e}} : \bar{\mathbf{S}}_{\mathbf{N}})}{\partial \mathbf{C}_{\mathbf{N}}^{\mathbf{e}}} + \frac{1}{2} \frac{\partial (\bar{\mathbf{S}}_{\mathbf{N}})}{\partial \theta}\right] : \dot{\mathbf{C}}_{\mathbf{N}}^{\mathbf{e}} + \\ &\theta \left[\frac{3}{2} f_\theta \mathbf{F}_{\mathbf{V}}^{\nu} \bar{\mathbf{S}}_{\mathbf{V}} \mathbf{F}_{\mathbf{V}}^{\nu \mathbf{T}} - f_\theta \frac{\partial \left(\mathbf{F}_{\mathbf{V}}^{\nu \mathbf{T}} \mathbf{C}_{\mathbf{V}}^{\mathbf{e}} \mathbf{F}_{\mathbf{V}}^{\nu} : \bar{\mathbf{S}}_{\mathbf{V}}\right)}{\partial \mathbf{C}_{\mathbf{V}}^{\mathbf{e}}} + \frac{1}{2} \frac{\partial \left(\mathbf{F}_{\mathbf{V}}^{\nu} \bar{\mathbf{S}}_{\mathbf{V}} \mathbf{F}_{\mathbf{V}}^{\nu \mathbf{T}}\right)}{\partial \theta}\right] : \dot{\mathbf{C}}_{\mathbf{V}}^{\mathbf{e}} - \bar{\nabla}_{\mathrm{x}} \bar{\mathbf{Q}} + \bar{\mathrm{R}} \end{aligned} \tag{11}$$

where $\bar{C}$ is the heat capacity per unit volume.

2.4. Intermolecular and network resistances: thermo-viscoplasticty

Intermolecular resistance

The intermolecular contribution to the Cauchy stress is defined by a temperature-dependent Neo-Hookean model as:

$$\boldsymbol{\sigma}_{\mathbf{I}} = \frac{\lambda_0(\theta) \ln(\mathrm{J}_{\mathrm{I}}^{\mathrm{e}}) \mathbf{I}}{\mathrm{J}_{\mathrm{I}}} + \frac{\mu_0(\theta)}{\mathrm{J}_{\mathrm{I}}} (\mathbf{F}_{\mathbf{I}}^{\mathbf{e}} \mathbf{F}_{\mathbf{I}}^{\mathbf{eT}} - \mathbf{I}) \tag{12}$$

where λ_0 and μ_0 are the classical Lamé constants linearly depending on temperature through the Young's modulus $\mathrm{E}(\theta) = \mathrm{E}_{\mathrm{ref}} + \mathrm{E}_1(\theta - \theta_{\mathrm{ref}})$ [45,50].

The plastic contribution is activated when a yield criterion $\mathrm{f}_{\mathrm{I}} = \bar{\bar{\sigma}}_{\mathrm{eqI}} - \sigma_{\mathrm{T}} = 0$ is satisfied. Here, the Rhagava equivalent stress $\bar{\bar{\sigma}}_{\mathrm{eqI}} = \frac{(\alpha-1)\mathrm{I}_{1\mathrm{I}} + \sqrt{(\alpha-1)^2 {\mathrm{I}_{1\mathrm{I}}}^2 + 12\alpha \mathrm{J}_{2\mathrm{I}}}}{2\alpha}$ is used to include the pressure dependency in the yield function [51]. Where α is a material parameter describing the pressure sensitivity and $\mathrm{I}_{1\mathrm{I}} = \mathrm{tr}\, \bar{\bar{\mathbf{M}}}_{\mathbf{I}}$ and $\mathrm{J}_{2\mathrm{I}} = \frac{1}{2} \bar{\bar{\mathbf{M}}}_{\mathbf{I}}^{\mathbf{dev}} : \bar{\bar{\mathbf{M}}}_{\mathbf{I}}^{\mathbf{dev}}$ are stress invariants of the Mandel stress tensor $\bar{\bar{\mathbf{M}}}_{\mathbf{I}} = \mathbf{C}_{\mathbf{I}}^{\mathbf{e}} \bar{\bar{\mathbf{S}}}_{\mathbf{I}}$ expressed in the $\bar{\bar{\Omega}}$. The scalar term $\sigma_{\mathrm{T}} = \sigma_{\mathrm{T0}} \left(1 - \left(\frac{\theta - \theta_{\min}}{\theta_{\mathrm{melt}} - \theta_{\min}}\right)^{\mathrm{m}}\right)$ is defined depending on temperature, where σ_{T0} is the value of σ_{T} at reference temperature in uniaxial tension, m is a temperature sensitivity parameter, $\theta_{\min}$ is the lowest temperature considered and θ_{melt} is the melting temperature.

The flow equation that describes the evolution of the plastic deformation is expressed in the plastic dilated relaxed configuration $\bar{\bar{\Omega}}$ as:

$$\bar{\bar{\mathbf{L}}}_{\mathbf{I}}^{\mathbf{p}} = \dot{\bar{\bar{\gamma}}}_{\mathrm{I}}^{\mathrm{p}} \bar{\bar{\mathbf{r}}}_{\mathbf{I}}; \qquad \bar{\bar{\mathbf{r}}}_{\mathbf{I}} = \frac{\partial g_{\mathrm{I}}}{\partial \bar{\bar{\mathbf{M}}}_{\mathbf{I}}} \tag{13}$$

where $\dot{\bar{\bar{\gamma}}}_{\mathrm{I}}^{\mathrm{p}}$ is the viscoplastic multiplier, $\bar{\bar{\mathbf{r}}}_{\mathbf{I}}$ is the gradient of the plastic potential $g_{\mathrm{I}} = \frac{(\beta-1)I_{1\mathrm{I}} + \sqrt{(\beta-1)^2 {I_{1\mathrm{I}}}^2 + 12\beta J_{2\mathrm{I}}}}{2\beta}$ on $\bar{\bar{\Omega}}$, with β being a parameter which controls the volumetric plastic strain.

The viscoplastic multiplier $\dot{\bar{\bar{\gamma}}}_{\mathrm{I}}^{\mathrm{p}}$ is defined depending on the rate-sensitivity parameters $\dot{\varepsilon}_0$ and C as:

$$\dot{\bar{\bar{\gamma}}}_{\mathrm{I}}^{\mathrm{p}} = \begin{cases} 0 & \text{if } f_{\mathrm{I}} \leq 0 \\ \dot{\varepsilon}_0 \left\{ \exp\left[\frac{1}{C} \left(\frac{\bar{\bar{\sigma}}_{\mathrm{eqI}}}{\sigma_{\mathrm{T}}} - 1 \right) \right] - 1 \right\} & \text{if } f_{\mathrm{I}} > 0 \end{cases} \tag{14}$$

Network resistance

This part of the model describes a hyperelastic entropic resistance defined by a modification of the originally eight-chain model proposed by Arruda and Boyce [52]. This modification follows the formulation introduced by Anand [53] but including temperature sensitivity. The Cauchy stress associated to this resistance is defined as:

$$\boldsymbol{\sigma}_{\mathbf{N}} = \frac{(C_{\mathrm{R}} + C_{\theta}(\theta - \theta_{\mathrm{ref}}))}{3J_{\mathrm{N}}} \frac{\bar{\lambda}_{\mathrm{L}}}{\bar{\lambda}} \mathfrak{L}^{-1}\left(\frac{\bar{\lambda}}{\bar{\lambda}_{\mathrm{L}}} \right) (\mathbf{B}_{\mathbf{N}}^{*} - \bar{\lambda}^2 \mathbf{I}) \tag{15}$$

where $\mathfrak{L}^{-1}$ is the inverse of the Langevin function, C_{R} is the initial elastic modulus of the network backstress resistance, C_{θ} is a material parameter controling the elastic modulus dependence on temperature and $\bar{\lambda}_{\mathrm{L}}$ is the locking stretch. $\bar{\lambda} = \sqrt{\frac{1}{3} \mathrm{tr}(\mathbf{F}_{\mathbf{N}}^{\mathbf{e}*} (\mathbf{F}_{\mathbf{N}}^{\mathbf{e}*})^{\mathrm{T}})}$ is the average total stretch ratio, with $\mathbf{F}_{\mathbf{N}}^{\mathbf{e}*} = J_{\mathrm{N}}^{-1/3} \mathbf{F}_{\mathbf{N}}^{\mathbf{e}}$ being the distortional part of $\mathbf{F}_{\mathbf{N}}^{\mathbf{e}}$ and $J_{\mathrm{N}} = \det(\mathbf{F}_{\mathbf{N}}^{\mathbf{e}})$.

2.5. Viscous resistance: viscoelasticity

This part of the model describes a viscous material response related to the hardening induced by rate-dependent effects on network stretching. To define this constitutive branch, an eight-chain model is defined for the non-linear spring that depends on the elastic part of the deformation gradient associated with the viscous resistance. In addition, a viscous flow rule is introduced to define the contribution of the linear dashpot. This idea was originally proposed by Bergström and Boyce [54] for elastomers modelling. The Cauchy stress associated with the viscous resistance is defined as:

$$\boldsymbol{\sigma}_{\mathbf{V}} = \frac{C_{\nu}}{3J_{\mathrm{V}}} \frac{\bar{\lambda}_{\mathrm{VL}}}{\bar{\lambda}_{\mathrm{V}}} \mathfrak{L}^{-1}\left(\frac{\bar{\lambda}_{\mathrm{V}}}{\bar{\lambda}_{\mathrm{VL}}} \right) (\mathbf{B}_{\mathbf{V}}^{\mathbf{e}*} - \bar{\lambda}_{\mathrm{V}}^2 \mathbf{I}) \tag{16}$$

where C_ν and $\bar{\lambda}_{VL}$ are material parameters and the average viscous stretch ratio $\bar{\lambda}_V$ is calculated as:

$$\bar{\lambda}_V = \sqrt{\frac{1}{3}\mathrm{tr}(\mathbf{B}_\mathbf{V}^{\mathbf{e}*})} \tag{17}$$

The distortional left Cauchy-Green viscous deformation tensor, $\mathbf{B}_\mathbf{V}^{\mathbf{e}*}$, is determined by the distortional part of $\mathbf{F}_\mathbf{V}^{\mathbf{e}}$ defined by Eq. (19).

$$\mathbf{B}_\mathbf{V}^{\mathbf{e}*} = \mathbf{F}_\mathbf{V}^{\mathbf{e}*}(\mathbf{F}_\mathbf{V}^{\mathbf{e}*})^{\mathrm{T}} \tag{18}$$

$$\mathbf{F}_\mathbf{V}^{\mathbf{e}*} = J_V^{-1/3}\mathbf{F}_\mathbf{V}^{\mathbf{e}} \tag{19}$$

In order to define the viscous velocity gradient in the viscous dilated relaxed configuration $\tilde{\Omega}$, a viscoelastic flow rule is assumed following the formulation proposed by Bergström [55] as:

$$\tilde{\mathbf{L}}_\mathbf{V}^{\boldsymbol{\nu}} = \dot{\tilde{\gamma}}_V^{\nu}\tilde{\mathbf{N}}_\mathbf{V}; \quad \tilde{\mathbf{N}}_\mathbf{V} = \frac{\boldsymbol{\sigma}_\mathbf{V}^{\mathbf{dev}}}{\tau_V} \tag{20}$$

where $\dot{\tilde{\gamma}}_V^{\nu}$ is the viscoelastic multiplier, $\tilde{\mathbf{N}}_\mathbf{V}$ provides the direction of the viscoelastic flow, $\boldsymbol{\sigma}_\mathbf{V}^{\mathbf{dev}}$ is the deviatoric part of $\boldsymbol{\sigma}_\mathbf{V}$ and $\tau_V = \sqrt{\mathrm{tr}\left(\boldsymbol{\sigma}_\mathbf{V}^{\mathbf{dev}}\boldsymbol{\sigma}_\mathbf{V}^{\mathbf{dev}}\right)}$ is the effective stress driving the viscous flow.

The rate equation for viscous flow is given by:

$$\dot{\tilde{\gamma}}_V^{\nu} = \frac{\tau_V}{\sigma_{VT}} \tag{21}$$

where σ_{VT} is a material constant.

3. Identification of model parameters and model predictions

This section summarizes the correspondence of the model parameters with the mechanical response of semi-crystalline matrix materials and, then, the identification of the parameters for UHMWPE is presented. In addition, the parameters of the model are also identified for HDPE in order to compare the predictive capability of the model for polymers that present different deformation behaviour.

3.1. Baseline material

Polyethylene is a highly ductile polymer that can be subjected to large deformations without fracture. This polymer presents different commercial forms whose mechanical properties depend on variables such as crystallinity degree, molecular weight and type of branching: HDPE, low density polyethylene (LDPE), cross-linked polyethylene (PEX) and UHMWPE. Among these polyethylene types, UHMWPE is one of the most employed because of its wear resistance, biocompatibility and good mechanical properties [18]. This thermoplastic polymer exhibits yielding-dependence on strain rate and temperature, increasing the yield stress with strain rate and decreasing with temperature. In addition, this material presents strain-hardening after yield. Although UHMWPE has no clear glass transition, a melting temperature of 405-409 K is observed

[22,56,57] and a thermal expansion coefficient of $124.5 \cdot 10^6$ K^{-1} [13]. In addition, these polymers allow for enhancing their mechanical properties through a wide range of fillers [15].

3.2. Correspondence of the model parameters with mechanical response of the material

The parameters of the proposed model present correspondence with the mechanical response of the material. This makes it easier to identify the proper values for a specific polymer. Such correspondence is introduced in terms of the following blocks:

(i) *Linear response*: the model parameters E_{ref}, E_1 and ν determine the initial elastic response of the material depending on temperature.

(ii) *Yield stress*: the parameters σ_{T0}, C, $\dot{\varepsilon}_0$ and m define the yield stress of the material. C and $\dot{\varepsilon}_0$ determine the yield stress' strain rate sensitivity and m the temperature sensitivity.

(iii) Viscous response: the model parameters C_ν and $\bar{\lambda}_{VL}$ determine the stress contribution of the spring of the viscous constitutive branch. C_ν is related to the initial elastic modulus of viscous resistance and $\bar{\lambda}_{VL}$ is related to the maximum (fully extended) stretch that a molecule can be exposed to. The material parameter σ_{VT} along with the stress state determines the viscoelastic multiplier that governs the flow rule associated with the linear dashpot.

(iv) *Network response*: the network contribution to the stress state is established by the parameters C_R, C_θ, $\bar{\lambda}_L$ and κ. C_R and C_θ determine the initial elastic modulus of network resistance depending on temperature. The parameter $\bar{\lambda}_L$ is related to the maximum stretch that a molecule can be exposed to and κ is a bulk modulus used in applications where only the network contribution is active (e.g. rubber modelling).

(v) *Volumetric plastic strain sensitivity*: the parameter β introduces the sensitivity of the material with inelastic volume change. This parameter can be defined as $\beta = 1$ assuming volume preserving.

(vi) *Stress state sensitivity*: the parameter α represents the relationship between yield stress in compression and tension and determines the pressure sensitivity.

Taking into account the correspondence of the model parameters with the mechanical response of the material, the parameters of the proposed model are identified for UHMWPE. For this identification process, experimental data covering a wide range of strain rate and temperature loading conditions is used. This experimental data and details about the experiments performance are reported by Brown et al. [18]. The model parameters identified from these experiments are provided in Table 1.

As UHMWPE, HDPE also exhibits yielding-dependence on strain rate and temperature. However, while UHMWPE or others polymers like PEX exhibit significant strain hardening after yield, other polymers such as HDPE present flat flow behaviour [18]. In order to compare the predictive capability of the model for different semi-crystalline polymers and to analyse the effects of particular deformation mechanisms on the mechanical response of these polymers, the model parameters are also identified for HDPE, Table 2.

Table 1
Material parameters for UHMWPE.

Initial elastic properties			Intermolecular resistance								
E_{ref} (GPa)	E_1 (MPa/K)	ν	$\dot{\varepsilon}_0$ (s^{-1})	C	σ_{T0} (MPa)	m	θ_{ref} (K)	θ_{melt} (K)	θ_{min} (K)	α	β
0.541	-6.5	0.46	0.1	0.048	37.5	0.7	293	406	198	1.0	1.0

Viscous resistance			Network resistance		
C_V (Pa)	$\bar{\lambda}_{VL}$	σ_{VT} (MPa)	C_R (MPa)	C_θ (MPa/K)	$\bar{\lambda}_L$
12.5	5	0.05	23	-0.15	5

General properties		
ρ (kg/m^3)	Cp (J/Kg K)	α_θ (K^{-1})
940	1900	$124.5 \cdot 10^{-6}$

Table 2
Material parameters for HDPE.

Initial elastic properties			Intermolecular resistance								
E_{ref} (GPa)	E_1 (MPa/K)	ν	$\dot{\varepsilon}_0$ (s^{-1})	C	σ_{T0} (MPa)	m	θ_{ref} (K)	θ_{melt} (K)	θ_{min} (K)	α	β
0.782	-6.5	0.46	0.01	0.028	80	0.76	293	406	198	1.0	1.0

Viscous resistance			Network resistance		
C_V (Pa)	$\bar{\lambda}_{VL}$	σ_{VT} (Pa)	C_R (MPa)	C_θ (MPa/K)	$\bar{\lambda}_L$
(-)	(-)	(-)	12	-0.15	5

General properties		
ρ (kg/m^3)	Cp (J/Kg K)	α_θ (K^{-1})
970	1900	$93.6 \cdot 10^{-6}$

3.3. Model predictions

In this section, the model predictions are compared with experimental data for a wide range of strain rate and temperature conditions. The constitutive model proposed herein is implemented in a VUMAT subroutine and applied to a numerical model with the dimensions of the specimens used in compression tests by Brown et al. [18]. This numerical model was defined with C3D8R elements and developed in Abaqus/Explicit.

The expression developed for the determination of temperature evolution, Eq. (11), is reduced taking into account uniquely specific energy due to plastic dissipation of the intermolecular resistance; viscous dissipation of the viscoelastic resistance; and heat conduction. Thermoelastic coupling is neglected in line with published studies for thermoplastic polymers [19,45]. The temperature evolution is thus reduced to:

$$\dot{\theta} = \frac{\bar{\mathbf{M}}_{\mathbf{I}}:\bar{\mathbf{D}}^{\mathbf{p}}}{\bar{C}} + \frac{\bar{\mathbf{M}}_{\mathbf{V}}:\bar{\mathbf{D}}^{\mathbf{v}}}{\bar{C}} - \frac{\bar{\nabla}_{\mathbf{x}}\bar{\mathbf{Q}}}{\bar{C}} \tag{22}$$

The model predictions show a good agreement with experiments in terms of strain rate and temperature sensitivities [18]. In this regard, Figs. 4 and 5 show the yield stress model predictions depending on strain rate and temperature; and their comparison with the experimental values for UHMWPE and HDPE respectively. This predictive capacity is determined by the intermolecular constitutive branch that accounts for strain rate sensitivity through the viscoplastic flow rule, Eq. (13), and for temperature sensitivity through the term σ_T that introduced thermal softening in the viscoplastic multiplier through Eq. (14).

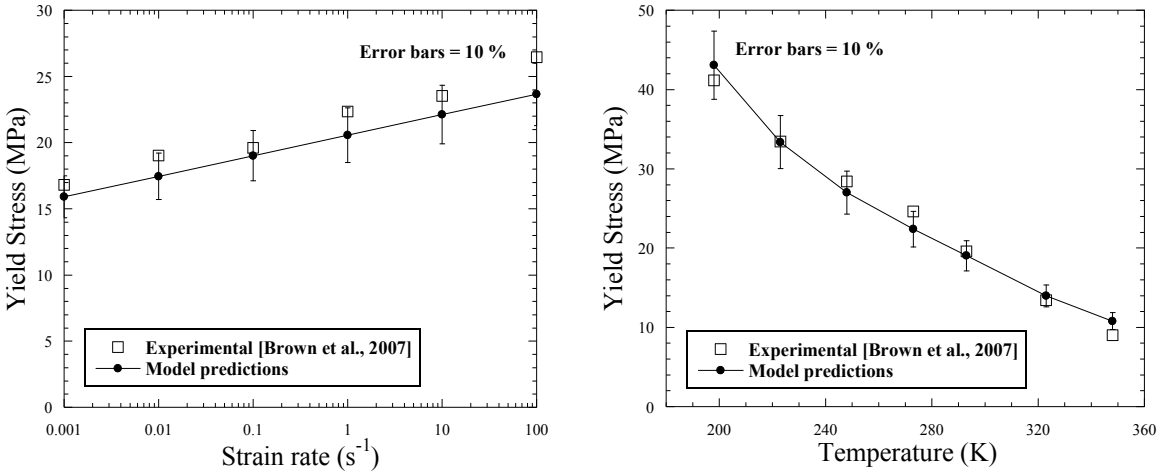

(a) (b)

Fig. 4. Experimental data [18] versus model predictions in terms of: (a) strain rate sensitivity; and (b) temperature sensitivity of UHMWPE for uniaxial compression tests.

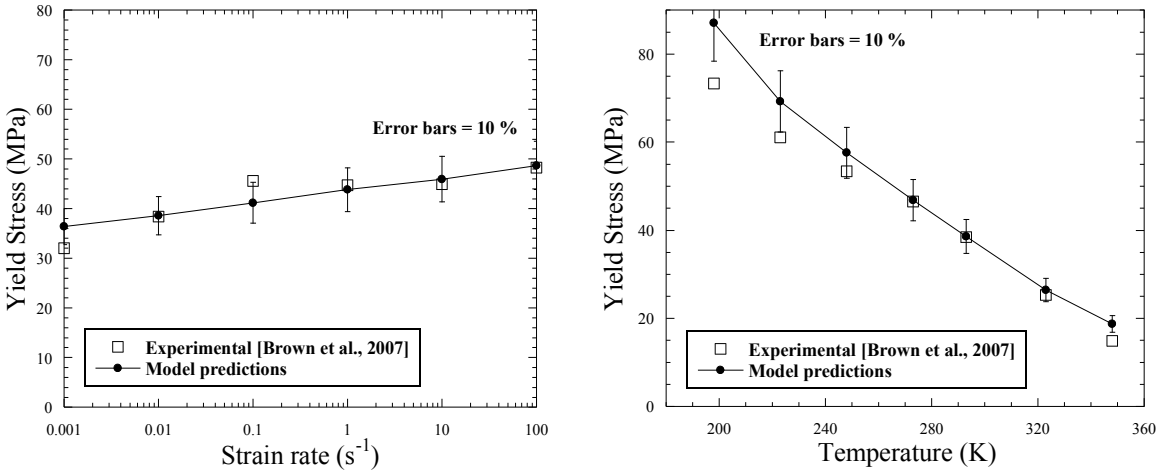

Fig. 5. Experimental data [18] versus model predictions in terms of: (a) strain rate sensitivity; and (b) temperature sensitivity of HDPE for uniaxial compression tests.

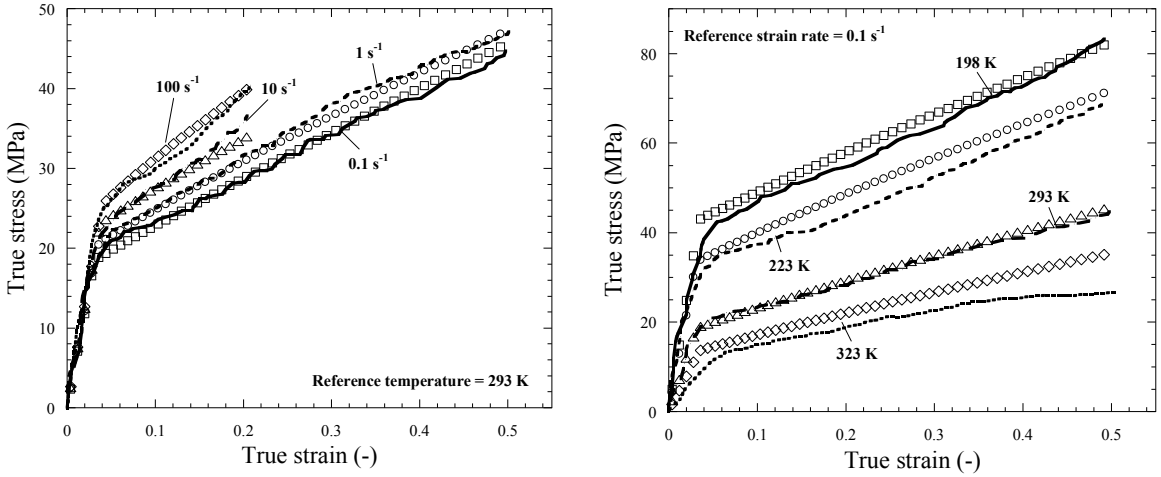

Fig. 6. Stress-strain experimental curves of UHMWPE [18] versus model predictions for: (a) different strain rates; and (b) different temperatures.

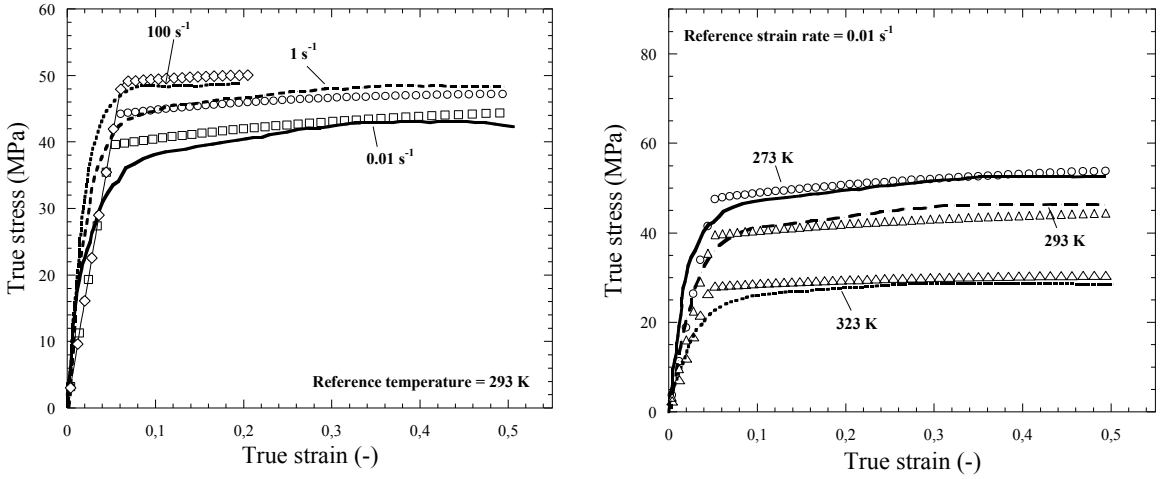

Fig. 7. Stress-strain experimental curves of HDPE [18] versus model predictions for: (a) different strain rates; and (b) different temperatures.

Furthermore, the model not only predicts the strain rate and temperature dependences on yield stress, but also on the stress response along the whole deformation process. With the aim of highlighting the predictive capacity of the proposed model, a comparison between model predictions and experimental data [18] is provided in Figs. 6 and 7. These figures show stress-strain curves for UHMWPE and HDPE covering a wide range of strain rate and temperature conditions. A good agreement between model predictions and experiments is observed in these terms. In this regard, the model faithfully predicts the initial slope of the stress-strain curve depending on temperature. This is determined by the definition of $E(\theta)$ in the intermolecular resistance. In addition, in the case of UHMWPE, once the yield point is reached, the stress-shape is mainly governed by the viscous and network resistances, especially at large deformations where their contribution is more relevant. The rate-dependent non-linear behaviour at large deformations is determined by the viscous resistance through the viscoelastic dashpot, Fig. 6a. Moreover, the network resistance introduces temperature dependence in the non-linear behaviour at large deformations, Fig. 6b. Unlike UHMWPE, the viscous flow of HDPE is defined uniquely by the intermolecular resistance since presents a linear behaviour without significant hardening after yielding, Fig. 7. Consequently, the viscoelastic branch was neglected here for HDPE.

Therefore, it can be concluded that the model allows for the introduction of temperature-dependent behaviour associated to both intermolecular and network resistances and couple viscoelastic and viscoplastic deformation mechanisms. This model, calibrated for different biomaterials, is potentially applied to problems in biomedical engineering allowing for the analysis of prosthesis devices that can be subjected to dynamic loading. In addition, the model offers other possibilities in terms of analysis of deformation mechanisms and their implications in semi-crystalline polymeric matrices, also allowing the extrapolation of results to a wider range of temperature and strain rate. In the next section, it is applied to the analysis of viscous behaviours and thermo-mechanical coupling on the deformation process of both polyethylene materials.

4. Analysis of viscous behaviours and thermo-mechanical coupling on necking

This section presents an analysis of the influence of viscous behaviours and deformation mechanisms on necking localization and temperature evolution due to inelastic dissipation. To this end, numerical simulations of tensile tests at different strain rate conditions were conducted.

4.1. Definition of the numerical model

A FE model of tensile specimen with a normalized ASTM D638 Type V geometry and 3 mm of thickness was developed, Fig. 8(a). The specimen presents a gauge section of 9.53 mm in length and 3.18 mm in width. This geometry was chosen in accordance with the specimens used by Mohagheghian et al. [58] in the experimental tensile tests carried out on HDPE and UHMWPE samples. A total number of 176,464 linear elements with reduced integration (C3D8R in Abaqus notation) were employed to mesh the whole region. A higher mesh density was defined in the central zone of the specimen, progressively decreasing the element size along the Z axis to the extremes of the specimen.

Regarding the boundary conditions, a constant stretching velocity is applied on one end face, while the nodes on the opposite face are embedded, Fig. 8 (b). These imposed loading conditions can be formulated as $V_Z(L_t, t) = \dot{\varepsilon}_0 \cdot L_0$ and $V_Z(0, t) = 0$ where t is the time, $\dot{\varepsilon}_0$ the initial strain

rate, L_t the specimen length and L_0 the gauge length. Note that the stretching velocity was defined assuming that the deformation localizes along the gauge length. Thus, the simulations were performed at two different strain rates, $\dot{\varepsilon}_0 = 0.1\ s^{-1}$ and $\dot{\varepsilon}_0 = 100\ s^{-1}$, allowing for evaluating the influence of this variable on material hardening and on thermo-mechanical coupling. Although an initial temperature of 293 K was defined for all simulations, it evolves along the deformation process due to the consideration of inelastic dissipation following Eq. (22). According to observations of other authors about temperature evolution for semi-crystalline polymers [19,59], Eq. (22) can be reduced neglecting the term associated to thermal conduction for high strain rate conditions assuming adiabatic heating.

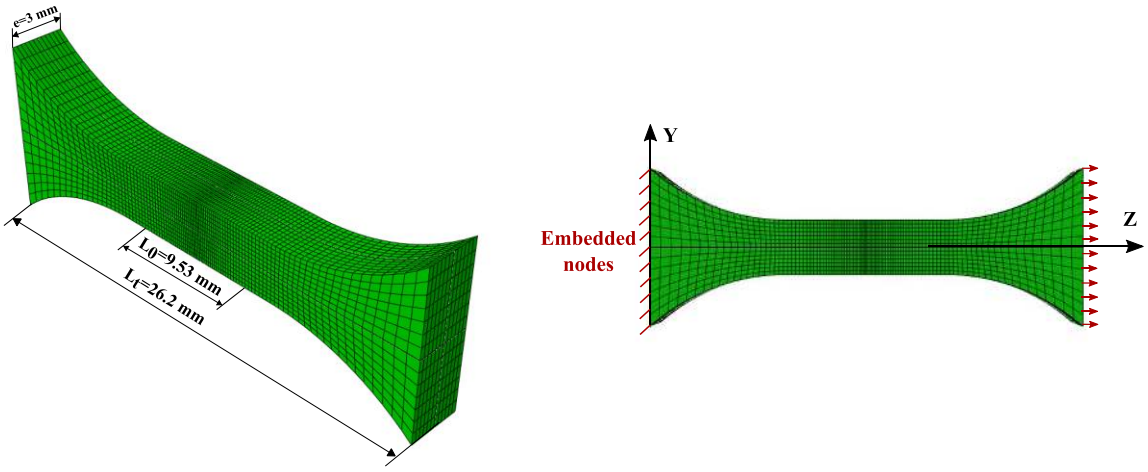

(a) (b)

Fig. 8. Numerical model: (a) geometrical information; (b) boundary conditions applied.

4.2. Results and analysis

A series of numerical simulations were performed to study and compare the influence of viscous-behaviours and thermo-mechanical coupling during the deformation process of two types of polyethylene. In these simulations, specimens of both materials were subjected to stretching conditions varying the initial strain rate. Experimentally, the mechanical behaviour of both materials presents a strong dependence on strain rate and temperature, increasing the yield stress with strain rate and decreasing with temperature. However, while the UHMWPE exhibits significant strain hardening after yield, Fig. 6, the HDPE presents flat flow behaviour Fig. 7. In the former, the viscoelastic resistance plays an important role in the deformation process, whereas in the HDPE this contribution is not relevant. In this regard, the mechanical response of these materials can be understood as the competition between hardening due to strain and strain rate effects and softening due to thermal effects. This competition becomes more complex at high strain rates where this variable induces an important hardening but thermal softening is more relevant because of the strong thermo-mechanical coupling under these conditions, as can be deduced from Eq. (22).

Figs. 9 and 10 show two stages of the tensile deformation process for UHMWPE and HDPE at strain rate conditions of 0.1 s^{-1} and 100 s^{-1}. These stages are identified by the engineering strain defined as $\varepsilon = \Delta Z/L_0$, where ΔZ is the current displacement applied in the longitudinal direction. A uniform deformation along the whole gauge length is observed for UHMWPE whereas HDPE presents a local deformation which results in a pronounced necking process. This difference in

the behaviour of both materials can be explained by the higher viscosity and strain-hardening after yield of UHMWPE with respect to HDPE. In this sense, viscous contributions to the mechanical behaviour have been demonstrated to stabilize necking formation leading to higher ductility [19]. Moreover, strain hardening also plays a stabilizing role in necking formation [58-60]. In addition, thermal softening also influences the deformation process of thermoplastic polymers [61-65], as observed in other ductile materials [66,67]. In this regard, understanding this as a negative hardening, if temperature evolution occurs heterogeneously by inelastic dissipation, local necking is favoured leading to instability in the zone that reaches higher temperatures. Fig. 11 shows the temperature distribution along the gauge length for both polyethylene materials at strains of 0.2 and 0.5 and strain rates of 0.1 s^{-1} and 100 s^{-1}. Temperature remains practically uniform along the gauge length of UHMWPE specimen whereas it shows a relevant concentration in the necking zone of HDPE specimen. This temperature increment due to inelastic dissipation is more relevant at high strain rates and leads to a more pronounced necking formation, see Fig. 10(d) where the temperature reaches a maximum up to $\Delta\theta = 60$ K in the necking zone of HDPE. Comparing the results in terms of temperature, a higher increment of this variable is reached by HDPE. Although this material does not present contribution of the viscous branch, the higher values of stress flow result in higher contribution of inelastic dissipation according to Eq. (22). This higher temperature increment in HDPE favours necking formation in comparison with UHMWPE.

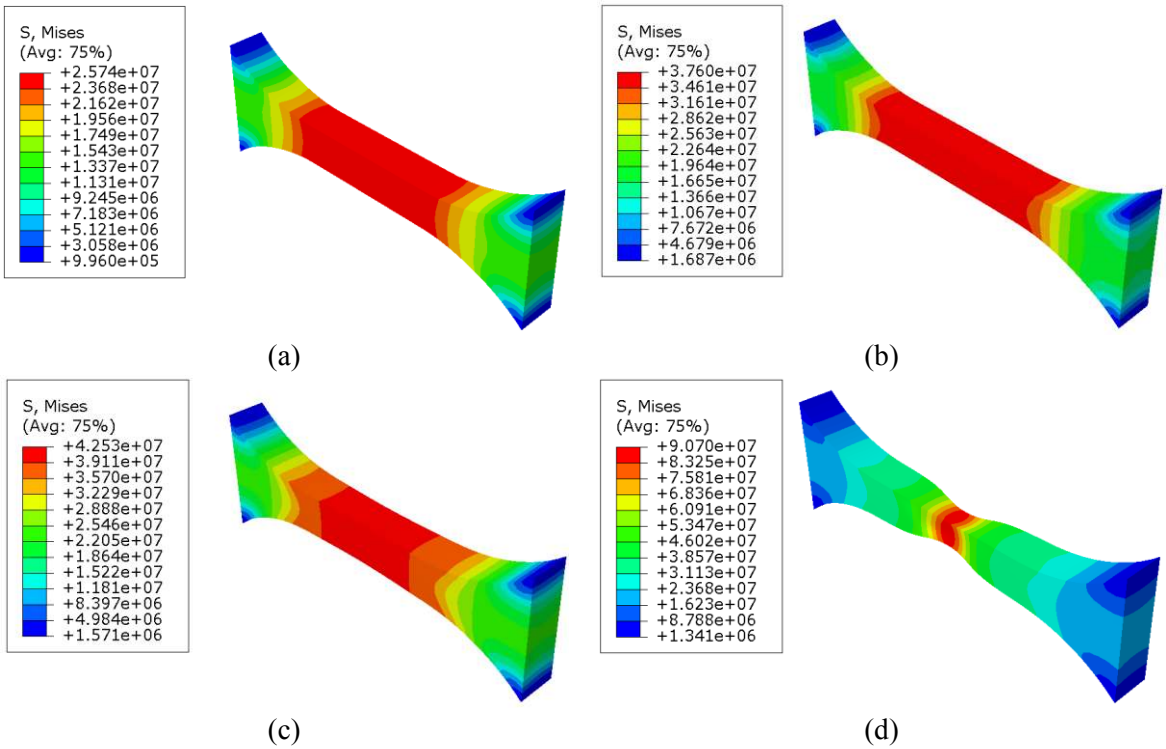

Fig. 9. Stress distribution at $\dot{\varepsilon}_0 = 0.1\ s^{-1}$ for: (a) UHMWPE at $\varepsilon = 0.2$ (b) UHMWPE at $\varepsilon = 0.5$ (c) HDPE at $\varepsilon = 0.2$ (d) HDPE at $\varepsilon = 0.5$.

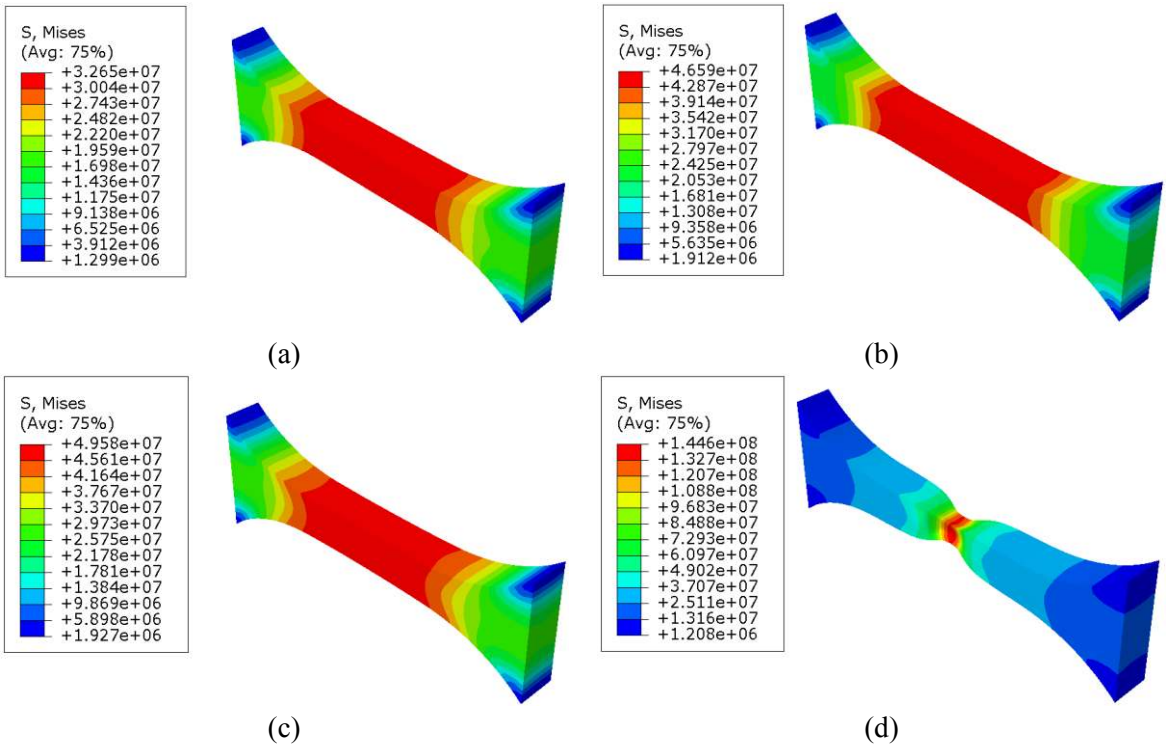

Fig. 10. Stress distribution at $\dot{\varepsilon}_0 = 100\ s^{-1}$ for: (a) UHMWPE at $\varepsilon = 0.2$ (b) UHMWPE at $\varepsilon = 0.5$ (c) HDPE at $\varepsilon = 0.2$ (d) HDPE at $\varepsilon = 0.5$.

The results numerically obtained here in terms of necking formation correlate with experiments conducted by others authors [58,59]. Mohagheghian et al. [58] studied the response of different types of polyethylene at nominal strain rates of $0.01\ s^{-1}$, $0.1\ s^{-1}$ and $1\ s^{-1}$ over specimens with the same geometry used in our numerical simulations. At low strain rates, HDPE presents neck formation while at high strain rates HDPE fails during neck propagation phases. In contrast, no necking process was showed in the UHMWPE specimen for all strain rates studied. This response was explained by the stabilising effect associated to strain hardening. Moreover, the same way to deform was observed by Torres et al. [68] for HDPE. These authors also observed a necking process with an increase in temperature along necking length in agreement with the results obtained here.

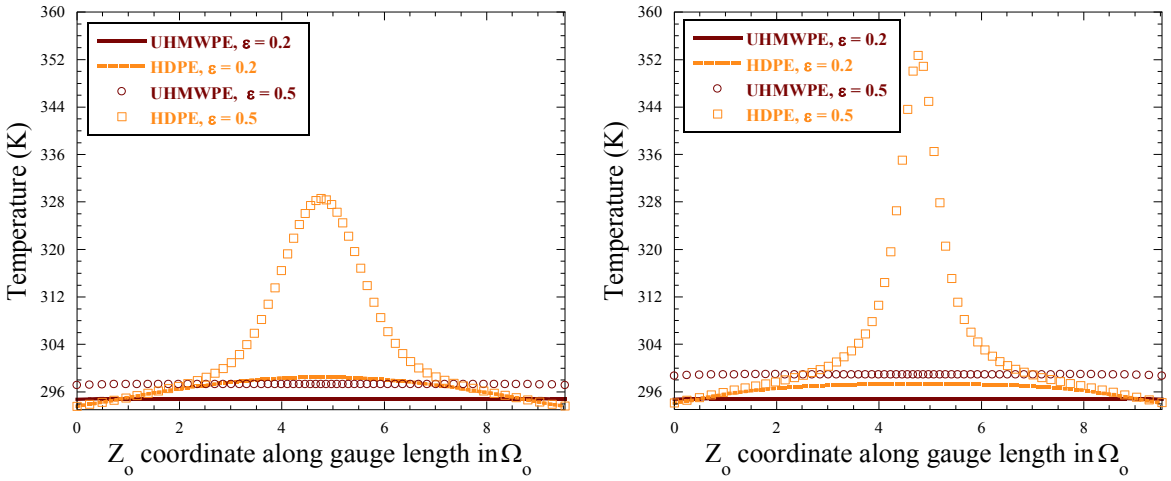

Fig. 11. Temperature distribution along gauge length at strains of 0.2 and 0.5 in UHMWPE and HDPE specimens at: (a) strain rate of 0.1 s^{-1}; and (b) strain rate of 100 s^{-1}.

5. Conclusions

In this work, a hyperelastic constitutive model which combines viscoelasticity and viscoplasticity with thermo-mechanical coupling is developed to predict the mechanical behaviour of semi-crystalline polymeric matrices. This model is physically motivated on the interpretation of the stress-strain response of semi-crystalline polymers as the combination of overcoming an intermolecular resistance, a viscous resistance and a network resistance. To this end, the intermolecular resistance introduces the thermo-viscoplastic behaviour of the polymer and the viscous and network resistances introduce the thermo-viscoelastic behaviour. In addition, temperature evolution due to inelastic dissipation is accounted for, as well as thermal softening associated to temperature increment.

The constitutive equations were implemented in a VUMAT subroutine for Abaqus/Explicit and then, the model parameters were identified for UHMWPE and HDPE from experimental data covering a wide range of strain rate and temperature conditions. Finally, the model was employed to study the influence of viscous contributions and thermo-mechanical coupling on necking process when semi-crystalline specimens are subjected to large stretching conditions. Numerical predictions show that UHMWPE can undergo higher strain values without neck formation leading to higher ductility with respect to HDPE.

The consideration of viscous behaviours and their thermo-mechanical coupling in the constitutive modelling of semi-crystalline polymers were identified as key points in the faithful prediction of the characteristic mechanical behaviour of both injection moulded and 3D printed thermoplastic polymers. In this sense, the constitutive model developed in this work is able not only to be considered as a predictive tool, but also to be useful in the understanding of the material behaviour of semi-crystalline polymers. The proposed model provides insights into the mechanical behaviour of polymeric matrices, allowing for the development of new composite materials with dynamic applications.

Acknowledgements

The researchers are indebted to the *Ministerio de Economía y Competitividad de España* (Project DPI2014-57989-P) for the financial support which permitted to conduct part of this work.
The authors acknowledge useful discussions with Prof. R. Zaera on the constitutive formulation of the model developed in this work. The authors also acknowledge useful discussions and clinical material provided by Dra. Inmaculada Gómez Arrayás, Specialist in Orthopaedic Surgery and Traumatology in the Hospital Ruber Internacional of Madrid.

Appendix A. Nomenclature used in the formulation

Nomenclature			
$\{\Omega_o, \bar{\Omega}, \bar{\bar{\Omega}}, \tilde{\Omega}, \Omega\}$	initial, dilated, plastic dilated relaxed, viscous dilated relaxed and current configurations	$\bar{\bar{\mathbf{W}}}_{\mathbf{I}}^{\mathbf{p}}$	skew part of the plastic velocity gradient in Ω
$\bar{e}$	specific internal energy per unit volume in $\bar{\Omega}$	$\tilde{\mathbf{W}}_{\mathbf{V}}^{\mathbf{v}}$	skew part of the viscous velocity gradient in $\tilde{\Omega}$
$\bar{\mathbf{Q}}$	heat flux per unit volume in $\bar{\Omega}$	$\boldsymbol{\sigma}$	Cauchy stress tensor
$\bar{R}$	heat resource per unit volume in $\bar{\Omega}$	$\boldsymbol{\sigma}_{\mathbf{N}}$	network Cauchy stress tensor
$\bar{\eta}$	specific entropy per unit volume in $\bar{\Omega}$	$\boldsymbol{\sigma}_{\mathbf{I}}$	intermolecular Cauchy stress tensor
$\bar{C}$	heat capacity per unit volume in $\bar{\Omega}$	$\boldsymbol{\sigma}_{\mathbf{V}}$	viscous Cauchy stress tensor
$\{\theta, \theta_{ref}, \theta_{melt}, \theta_{min}\}$	current, reference, melting and lowest temperature considered	$\bar{\mathbf{S}}_{\mathbf{N}}$	network second Piola-Kirchhoff stress tensor in $\bar{\Omega}$
f_θ	temperature-dependent function	$\{\bar{\mathbf{S}}_{\mathbf{I}}, \bar{\bar{\mathbf{S}}}_{\mathbf{I}}\}$	intermolecular second Piola-Kirchhoff stress tensor in $\bar{\Omega}$ and $\bar{\bar{\Omega}}$
$\bar{\Psi}$	Helmholtz free energy per unit volume in $\bar{\Omega}$	$\bar{\mathbf{S}}_{\mathbf{V}}$	viscous second Piola-Kirchhoff stress tensor in $\bar{\Omega}$
$\bar{\nabla}_x$	gradient with respect to the point x in $\bar{\Omega}$	$\bar{\mathbf{M}}_{\mathbf{N}}$	network Mandel stress tensor in $\bar{\Omega}$
$\mathfrak{L}$	Langevin function	$\{\bar{\mathbf{M}}_{\mathbf{I}}, \bar{\bar{\mathbf{M}}}_{\mathbf{I}}\}$	intermolecular Mandel stress tensor in $\bar{\Omega}$ and $\bar{\bar{\Omega}}$
$\mathbf{I}$	Identity matrix	$\bar{\mathbf{M}}_{\mathbf{V}}$	viscous Mandel stress tensor in $\bar{\Omega}$
J_I	determinant of the intermolecular deformation gradient	$\bar{\lambda}$	average total stretch ratio
J_N	determinant of the network deformation gradient	$\bar{\lambda}_L$	locking stretch
J_V	determinant of the viscous deformation gradient	$\{I_{1I}, J_{2I}\}$	stress invariants of the intermolecular Mandel stress tensor
$\mathbf{F}$	deformation gradient	$\bar{\bar{\sigma}}_{eqI}$	Rhagava equivalent stress
$\mathbf{F}^{\boldsymbol{\theta}}$	thermal deformation gradient	g_I	plastic potential
$\mathbf{F}^{\mathbf{M}}$	mechanical deformation gradient	$\bar{\bar{\mathbf{r}}}_{\mathbf{I}}$	gradient of the plastic potential
$\mathbf{F}_{\mathbf{N}}^{\mathbf{e}}$	network elastic deformation gradient	$\dot{\bar{\gamma}}_I^p$	viscoplastic multiplier
$\mathbf{F}_{\mathbf{I}}^{\mathbf{e}}$	intermolecular elastic deformation gradient	α_θ	thermal expansion coefficient
$\mathbf{F}_{\mathbf{I}}^{\mathbf{p}}$	intermolecular plastic deformation gradient	$\{\lambda_0, \mu_0\}$	classical Lamé constants
$\mathbf{F}_{\mathbf{V}}^{\mathbf{e}}$	viscoelastic elastic deformation gradient	E	Young's modulus
$\mathbf{F}_{\mathbf{V}}^{\mathbf{v}}$	viscoelastic viscous deformation gradient	$\{E_{ref}, E_1\}$	Young's modulus at the reference temperature and a specified material parameter
$\{\mathbf{C}_{\mathbf{N}}^{\mathbf{e}}, \mathbf{B}_{\mathbf{N}}^{\mathbf{e}}\}$	network elastic right and left Cauchy-Green tensor	$\{\sigma_T, \sigma_{T0}\}$	yield stress in uniaxial tension and its value at reference temperature
$\mathbf{C}_{\mathbf{I}}^{\mathbf{e}}$	intermolecular elastic right Cauchy-Green tensor	α	pressure sensitivity parameter
$\{\mathbf{C}_{\mathbf{V}}^{\mathbf{e}}, \mathbf{B}_{\mathbf{V}}^{\mathbf{e}}\}$	viscous elastic right Cauchy-Green tensor	β	volumetric plastic strain parameter
$\mathbf{l}$	velocity gradient	$\dot{\varepsilon}_0$	reference strain rate
$\mathbf{l}_{\mathbf{V}}^{\mathbf{e}}$	viscous elastic velocity spatial gradient	C	rate sensitivity parameter

$\bar{\mathbf{L}}^{\boldsymbol{\theta}}$	thermal velocity gradient in $\bar{\Omega}$	m	temperature sensitivity parameter
$\tilde{\mathbf{L}}_{\mathbf{V}}^{\boldsymbol{\nu}}$	viscous velocity gradient in $\tilde{\Omega}$	C_R	initial elastic modulus of the network backstress resistance
$\bar{\bar{\mathbf{L}}}_{\mathbf{I}}^{\mathbf{p}}$	plastic velocity gradient in $\bar{\bar{\Omega}}$	C_θ	temperature-dependent material parameter controlling the elastic modulus of network
$\mathbf{d}_{\mathbf{N}}^{\mathbf{e}}$	symmetric part of the network elastic velocity gradient in Ω	C_ν	initial elastic modulus of the viscous backstress resistance
$\mathbf{d}_{\mathbf{I}}^{\mathbf{e}}$	symmetric part of the intermolecular elastic velocity gradient in Ω	$\bar{\lambda}_V$	average viscous stretch ratio
$\mathbf{d}_{\mathbf{V}}^{\mathbf{e}}$	symmetric part of the viscous elastic velocity gradient in Ω	$\bar{\lambda}_{VL}$	viscous locking stretch
$\bar{\mathbf{D}}^{\mathbf{p}}$	symmetric part of the plastic velocity gradient in $\bar{\Omega}$	$\tilde{\mathbf{N}}_{\mathbf{V}}$	gradient of the viscoelastic flow
$\bar{\mathbf{D}}^{\boldsymbol{\nu}}$	symmetric part of the viscous velocity gradient in $\bar{\Omega}$	$\dot{\tilde{\gamma}}_V^{\nu}$	viscoelastic multiplier
$\bar{\bar{\mathbf{D}}}_{\mathbf{I}}^{\mathbf{p}}$	symmetric part of the intermolecular plastic velocity gradient in $\bar{\bar{\Omega}}$	τ_V	effective stress driving the viscous flow
$\tilde{\mathbf{D}}_{\mathbf{V}}^{\boldsymbol{\nu}}$	symmetric part of the intermolecular viscous velocity gradient in $\tilde{\Omega}$	σ_{VT}	Material parameter of the viscous resistance
$\bar{\mathbf{W}}^{\boldsymbol{\theta}}$	skew part of the thermal velocity gradient in $\bar{\Omega}$		

REFERENCES

[1] Chukov DI, Stepashkin AA, Maksimkin AV, Tcherdyntsev VV, Kaloshkin SD, Kuskov KV, Bugakov VI. Investigation of structure, mechanical and tribological properties of short carbon fiber reinforced UHMWPE-matrix composites. Compos Part B Eng 2015;76:79–88.

[2] Shrama S, Bijwe J, Panier S. Assessment of potential of nano and micro-sized boron carbide particles to enhance the abrasive wear resistance of UHMWPE. Compos Part B Eng 2016;99:312–320.

[3] Wood W, Maguire RG, Zhong WH. Improved wear and mechanical properties of UHMWPE–carbon nanofiber composites through an optimized paraffin-assisted melt-mixing process. Compos Part B Eng 2011;42:584-591.

[4] Savas LA, Tayfun U, Dogan M. The use of polyethylene copolymers as compatibilizers in carbon fiber reinforced high density polyethylene composites. Compos Part B Eng 2016;99;188-195.

[5] Chang B, Akil H, Nasir R, Khan A. Optimization on wear performance of UHMWPE composites using response surface methodology. Tribology International 2015; 88:252-262.

[6] Atkins GJ, Welldon KJ, Holding CA, Haynes DR, Howie DW, Findlay DM. The induction of a catabolic phenotype in human primary osteoblasts and osteocytes by polyethylene particles. Biomaterials 2009;30(22):3672–3681.

[7] Senatov FS, Gorshenkov MV, Tcherdyntsev VV, Kaloshkin SD, Sudarchikov VA. Fractographic analysis of composites based on ultra high molecular weight polyethylene. Compos Part B Eng 2014;56:869-875.

[8] Abdul-Hameed H, Messager T, Ayoub G, Zaïri F, Naït-Abdelaziz M, Qu Z, Zaïri F. A two-phase hyperelastic-viscoplastic constitutive model for semi-crystalline polymers: Application to polyethylene materials with a variable range of crystal fractions. J Mech Behav Biomater 2014;37:323–332.

[9] Wang X, Jiang M, Zhou Z, Gou J, Hui D. 3D printing of polymer matrix composites: A review and prospective. Compos Part B Eng 2017; 110:442-458.

[10] Singh D, Singh R, Boparai K, Farina I, Anita Kamra Verma A. In-vitro studies of SS 316 L biomedical implants prepared by FDM, vapor smoothing and investment casting. Compos Part B Eng 2018;132:107-114.

[11] Cheung H, Lau K, Lu T, Hui D. A critical review on polymer-based bio-engineered materials for scaffold development. Compos Part B Eng 2007;38(3):291-300.

[12] Garcia-Gonzalez D, Jayamohan J, Sotiropoulos N, H.Yoon H.Cook, Siviour C, Arias A, Jérusalem A. On the mechanical behaviour of PEEK and HA cranial implants under impact loading. J Mech Behav Biomater 2017;69:342-354.

[13] Affatato S, Ruggiero A, Merola M. Advanced biomaterials in hip joint arthroplasty. A review on polymer and ceramics composites as alternative bearings. Compos Part B Eng 2015;83:276–283.

[14] Fouad H, Elleithy R. High density polyethylene/graphite nano-composites for total hip joint replacements: processing and in vitro characterization. J Mech Behav Biomater 2011;4(7):1376–1383.

[15] Kurtz SM. UHMWPE biomaterials handbook ultra-high molecular weight polyethylene in total joint replacement and medical devices. 2nd ed. Elsevier; 2009.

[16] Fang L, Gao P, Leng Y. High strength and bioactive hydroxyapatite nano-particles reinforced ultrahigh molecular weight polyethylene. Compos Part B Eng 2007;38(3):345–351.

[17] Suñer S, Joffe R, Tipper JL, Emami N. Ultra high molecular weight polyethylene/graphene oxide nanocomposites: Thermal, mechanical and wettability characterization. Compos Part B Eng 2015;78:185–191.

[18] Brown EN, Willms RB, Gray III GT, Rae PJ, Cady CM, Vecchio KS, Flowers J, Martinez MY. Influence of Molecular Conformation on the Constitutive Response of Polyethylene: A Comparison of HDPE, UHMWPE, and PEX. Exp Mech 2007;47(3):381–393.

[19] Garcia-Gonzalez D, Zaera R, Arias A. A hyperelastic-thermoviscoplastic constitutive model for semi-crystalline polymers: Application to PEEK under dynamic loading conditions. Int J Plasticity 2017;88:27–52.

[20] Hachour K, Zaïri F, Naït-Abdelaziz M, Gloaguen JM, Aberkane M, Lefebvre JM. Experiments and modeling of high-crystalline polyethylene yielding under different stress states. Inter J Plasticity 2014;54:1–18.

[21] G'Sell C, Dahoun A. Evolution of microstructure in semicrystalline polymers under large plastic deformations. Mater Sci Eng A 1994:175;183–99.

[22] Bogetti TA, Walter M, Staniszewski J, Cline J. Interlaminar shear characterization of ultra-high molecular weight polyethylene (UHMWPE) composite laminates. Compos Part A-Appl S 2017;98:105–115.

[23] Walley SM, Field JE, Pope PH, Safford NA. A study of the rapid deformation behaviour of a range of polymers. Philos Trans R Soc London A 1989;328:1–33.

[24] Zeltmann S, Prakash K, Doddamani M, Gupta N. Prediction of modulus at various strain rates from dynamic mechanical analysis data for polymer matrix composites. Compos Part B: Eng 2017;120:27-34.

[25] Garg M, Mulliken AD, Boyce MC. Temperature rise in polymeric materials during high rate deformation. J Appl Mech 2008;75(1):011009.

[26] Arias A, Forquin P, Zaera R, Navarro C. Relationship between static bending and compressive behaviour of particle-reinforced composites. Compos Part B Eng 2008;39 (7-8): 1205-1215.

[27] Garcia-Gonzalez D, Rusinek A, Jankowiak T, Arias A. Mechanical impact behavior of polyether–ether–ketone (PEEK). Compos Struct 2015;124:88-99

[28] Garcia-Gonzalez D, Rodriguez-Millan M, Rusinek A, Arias A. Investigation of mechanical impact behavior of short carbon-fiber-reinforced PEEK composites. Compos Struct 2015;133:1116-1126.

[29] Garcia-Gonzalez D, Rodriguez-Millan M, Rusinek A, Arias A. Low temperature effect on impact energy absorption capability of PEEK composites. Compos Struct 2015;134:440-449.

[30] Hughes TJR. Numerical implementation of constitutive models: rate-independent deviatoric plasticity. In: S. Nemat-Nasser, R.J. Asaro. editors. Theoretical foundation for large-scale computations for nonlinear material behavior. Nijhoff Publishers, 1984.

[31] Bartel DL, Bicknell VL, Wright TM. The effect of conformity, thickness, and material on stresses in ultra-high molecular weight components for total joint replacement. J Bone Joint Surg Am 1986;68(7):1041–1051.

[32] Ishikawa H, Fujiki H, Yasuda K. Contact analysis of ultrahigh molecular weight polyethylene articular plate in artificial knee joint during gait movement. J Biomech Eng 1996;118(3):377–386.

[33] Kurtz SM, Jewett CW, Crane D, Pruitt L, Foulds JR, Edidin AA. Ultimate properties and crystalline morphology of ultra-high molecular weight polyethylene during uniaxial and biaxial tension. Trans 24th Soc Biomater 1998. p. 125.

[34] Bergström JS, Rimnac CM, Kurtz SM. An augmented hybrid constitutive model for simulation of unloading and cyclic loading behavior of conventional and highly crosslinked UHMWPE. Biomaterials 2004;25(11):2171–2178.

[35] Khan A, Zhang H. Finite deformation of polymer: experiments and modeling. Int J of Plasticity 2001;17:1167–1188.

[36] Bergström JS, Kurtz SM, Rimnac CM, Edidin AA. Constitutive modeling of ultra-high molecular weight polyethylene under large-deformation and cyclic loading conditions. Biomaterials 2002;23(11):2329–2343.

[37] Boyce MC, Arruda EM. Constitutive models of rubber elasticity: a review. Rubber Chem Technol 2000;73(3):504–523.

[38] Ahzi S, Makradi A, Gregory RV, Edie DD. Modeling of deformation behavior and strain-induced crystallization in poly(ethylene terephthalate) above the glass transition temperature. Mech Mater 2003;35(12):1139–1148.

[39] Ayoub G, Zaïri F, Naït-Abdelaziz M, Gloaguen JM. Modelling large deformation behaviour under loading-unloading of semicrystalline polymers: Application to a high density polyethylene. Int J Plast 2010;26(3):329–347.

[40] Dassault Systemes Abaqus v6.12 Documentation, 2012. ABAQUS Analysis User's Manual. Abaqus Inc.

[41] Yu JS, Maniatty AM, Knorr DB. Model for predicting thermal stresses in thin crystalline films. J Mech Phys Solids 1997;45(4):511–534.

[42] Kamlah M, Tsakmakis C. Use of isotropic thermoelasticity laws in finite viscoplasticity models. Continuum Mech Therm 1999;11(2):73–88.

[43] Boyce MC, Parks DM, Argon AS. Large inelastic deformation of glassy polymers. Part I: rate dependent constitutive model. Mech Mater 1988;7(1):15–33.

[44] Gurtin ME, Anand L. The decomposition F = FeFp, material symmetry, and plastic irrotationality for solids that are isotropic-viscoplastic or amorphous. Int J Plast 2005;21:1686–1719.

[45] Bouvard JL, Francis DK, Tschopp MA, Marin EB, Bammann DJ, Horstemeyer MF. An internal state variable material model for predicting the time, thermomechanical, and stress state dependence of amorphous glassy polymers under large deformation. Int J Plast 2013;42:168–193.

[46] Reese S. Multiplicative thermo-viscoplasticity: a thermodynamic model and its finite element implementation. Tech Mech 1998;18:209–216.

[47] Vladimirov IN, Pietryga MP, Reese S. Anisotropic finite elastoplasticity with nonlinear kinematic and isotropic hardening and application to sheet metal forming. Int J Plast 2010;26(5):659–687.

[48] Coleman BD, Noll W. The thermodynamics of elastic materials with heat conduction and viscosity. Arch Rational Mech Analysis 1963;13(1):167–178.

[49] Coleman BD, Gurtin ME. Thermodynamics with internal state variables. The J Chem Phys 1967;45:597.

[50] Rae PJ, Brown EN, Orler EB. The mechanical properties of poly(ether-ether-ketone) (PEEK) with emphasis on the large compressive strain response Polymer 2007;48(2):598–615.

[51] Raghava RS, Caddell RM. Macroscopic yield criterion for crystalline polymers. Int J Mech Sci 1973;15(12):967–974.

[52] Arruda EM, Boyce MC. A three-dimensional constitutive model for the large stretch behaviour of rubber elastic materials. J Mech Phys Solids 1993;41(2):389–412.

[53] Anand L. A constitutive model for compressible elastomeric solids. Comput Mech 1996;18(5):339–355.

[54] Bergström JS, Boyce MC. Constitutive modeling of the time-dependent and cyclic loading of elastomers and application to soft biological tissues. Mech Mater 2001;33(9):523–530.

[55] Bergström JS. Mechanics of Solid Polymers: theory and computational modeling, first ed. William Andrew, San Diego, USA, 2015.

[56] Sobieraj M, Kurtz S, Rimnac C. Notch strengthening and hardening behavior of conventional and highly crosslinked UHMWPE under applied tensile loading. Biomaterials 2005;26(17):3411–3426.

[57] Lim KLK, Ishak ZAM, Ishiaku US, Fuad AMY, Yusof AH, Czigany T, Pukanszky B, Ogunniyi DS. High-density polyethylene/ultrahigh-molecular-weight polyethylene blend. I. The processing, thermal, and mechanical properties. J Appl Polym Sci 2005;97:413–425.

[58] Mohagheghian I, McShane GJ, Stronge WJ. Impact perforation of monolithic polyethylene plates: Projectile nose shape dependence. Int J Impact Eng 2015;80:162–176.

[59] Hillmansen S, Haward RN. Adiabatic failure in polyethylene. Polymer 2001;42(22):9301–9312.

[60] Pęcherski R. Discussion of sufficient condition for plastic flow localization. Eng Fract Mech 1985;21(4):767-779.

[61] Segreti M, Rusinek A, Klepaczko J. Experimental study on puncture of PMMA at low and high velocities, effect on the failure mode. Polymer Testing 2004;23(6):703-718.

[62] Forquin P, Nasraoui M, Rusinek A, Siada L. Experimental study of the confined behaviour of PMMA under quasi-static and dynamic loadings. Int J Impact Eng 2012;40:46-57.

[63] Chalal H, Abed-Meraim F. Hardening effects on strain localization predictions in porous ductile materials using the bifurcation approach. Mech Mater 2015; 91:152–166.

[64] Nasraoui M, Forquin P, Siad L, Rusinek A. Influence of strain rate, temperature and adiabatic heating on the mechanical behaviour of poly-methyl-methacrylate: Experimental and modelling analyses. Mater Design 2012;37:500-509.

[65] Matadi-Boumbimba R, Froustey C, Viot P, Gerard P. Low velocity impact response and damage of laminate composite glass fibre/epoxy based tri-block copolymer. Compos Part B:Eng 2015;76:332–342.

[66] Rodriguez-Martinez JA, Rodríguez-Millan M, Rusinek A, Arias A. A dislocation-based constitutive description for modeling the behavior of FCC metals within wide ranges of strain rate and temperature. Mech Mater 2011;43(12):901-912.

[67] Rodriguez-Martinez JA, Pesci R, Rusinek A, Arias A, Zaera R, Pedroche D. Thermo-mechanical behaviour of TRIP 1000 steel sheets subjected to low velocity perforation by conical projectiles at different temperatures. Int J Solids Struct 2010;47(9):1268-1284.

[68] Torres JP, Frontini PM, Machado M, Major Z. Deformation and failure of semicrystalline polymers under dynamic tensile and biaxial impact loading. Int J Impact Eng 2016;98:52–61.

Figures

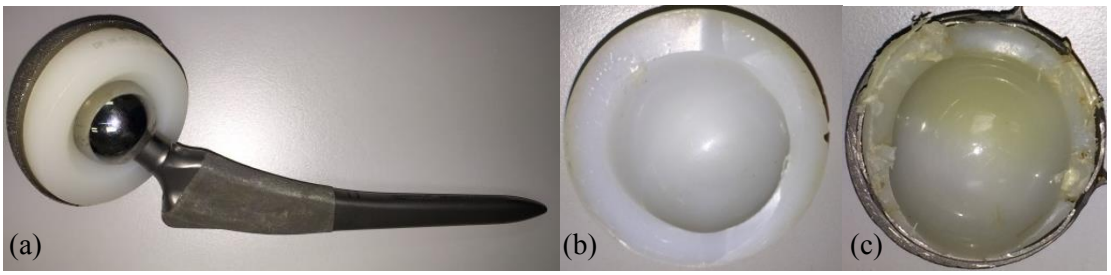

Fig. 1. (a) Real polyethylene-metal hip prosthetic. (b)-(c) Polyethylene acetabular cup removed from patients due to excessive material erosion. Materials provided by Dra. I. Gómez Arrayás (Hospital Ruber Internacional of Madrid).

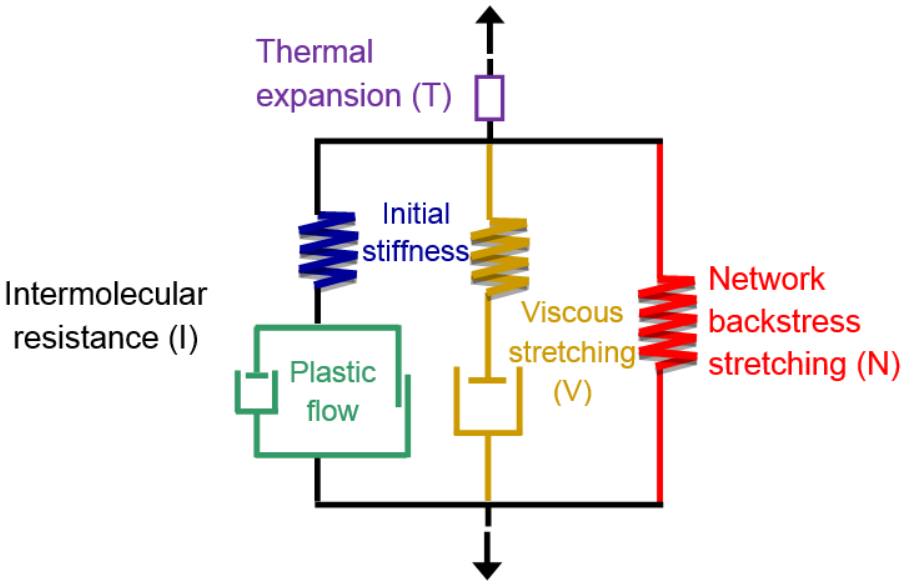

Fig. 2. Rheological scheme of the proposed constitutive model.

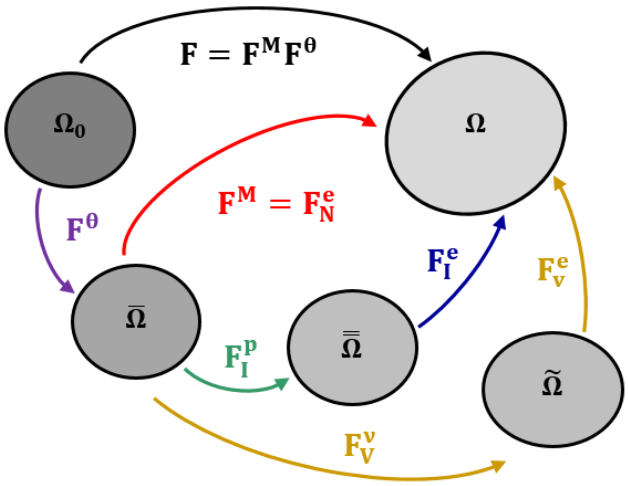

Fig. 3. Kinematics of the model showing the reference or initial configuration Ω_o, the dilated configuration $\bar{\Omega}$, the plastic dilated relaxed configuration $\bar{\bar{\Omega}}$, the viscous dilated relaxed configuration $\tilde{\Omega}$, and the current or loaded configuration Ω.

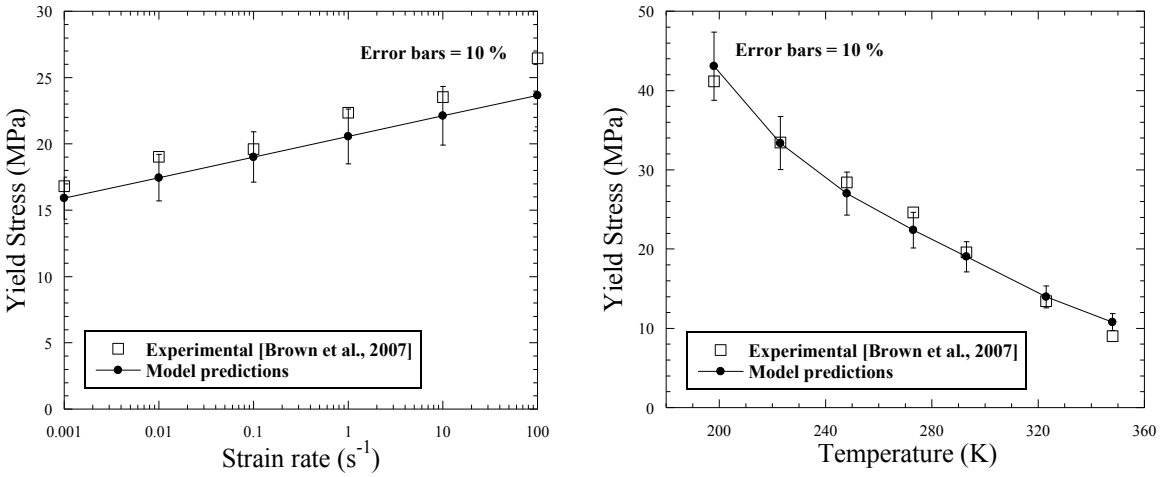

Fig. 4. Experimental data [18] versus model predictions in terms of: (a) strain rate sensitivity; and (b) temperature sensitivity of UHMWPE for uniaxial compression tests.

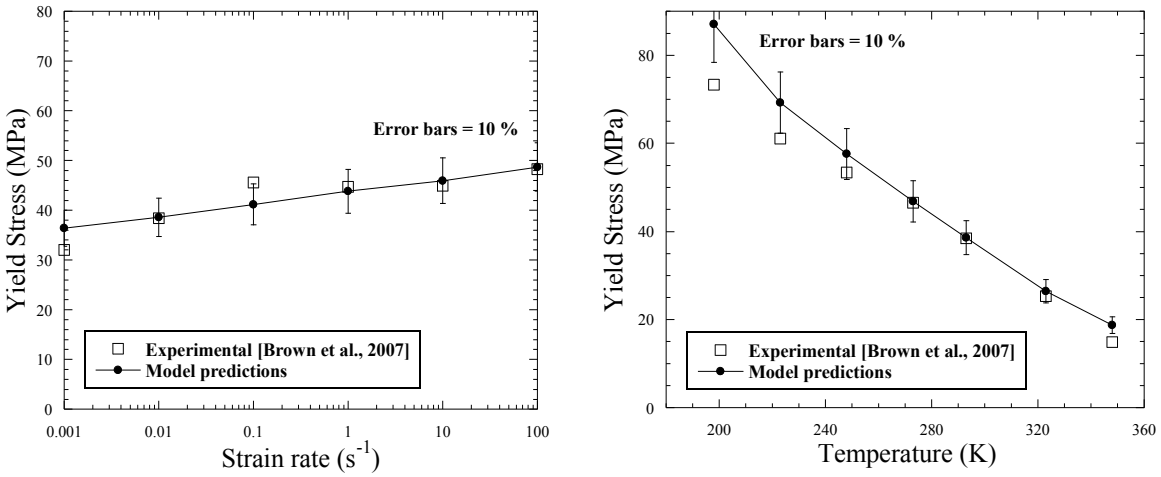

(a) (b)

Fig. 5. Experimental data [18] versus model predictions in terms of: (a) strain rate sensitivity; and (b) temperature sensitivity of HDPE for uniaxial compression tests.

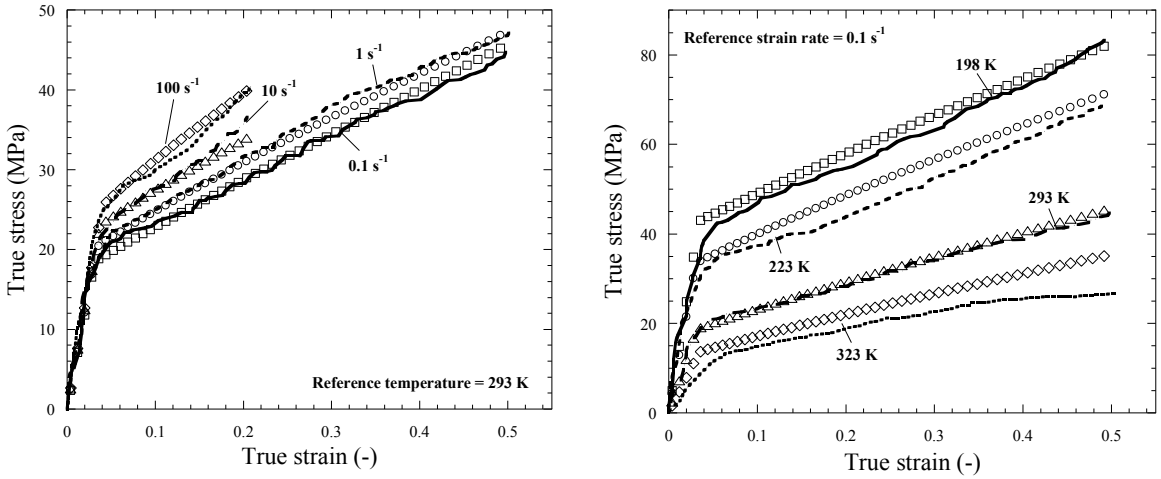

(a) (b)

Fig. 6. Stress-strain experimental curves of UHMWPE [18] versus model predictions for: (a) different strain rates; and (b) different temperatures.

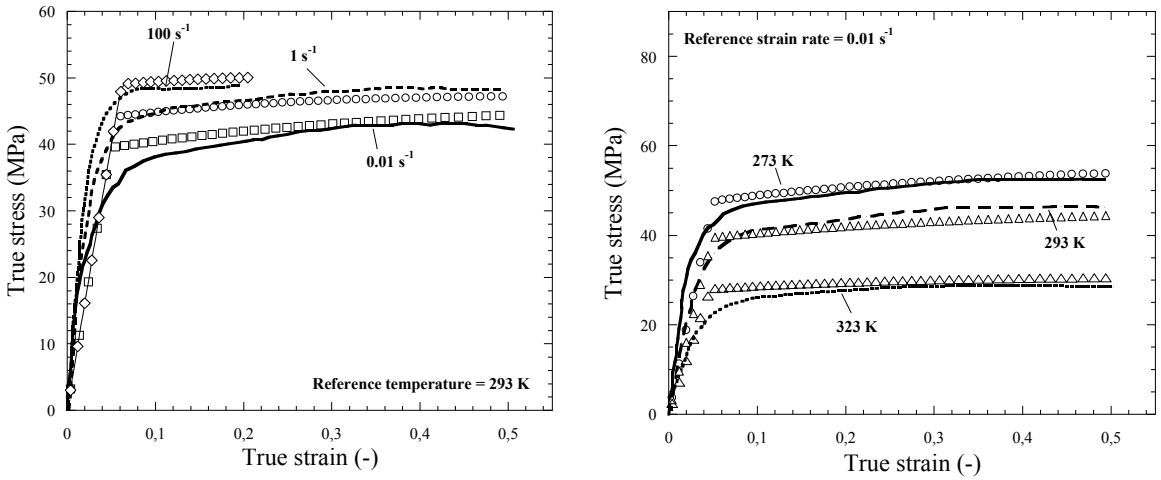

(a) (b)

Fig. 7. Stress-strain experimental curves of HDPE [18] versus model predictions for: (a) different strain rates; and (b) different temperatures.

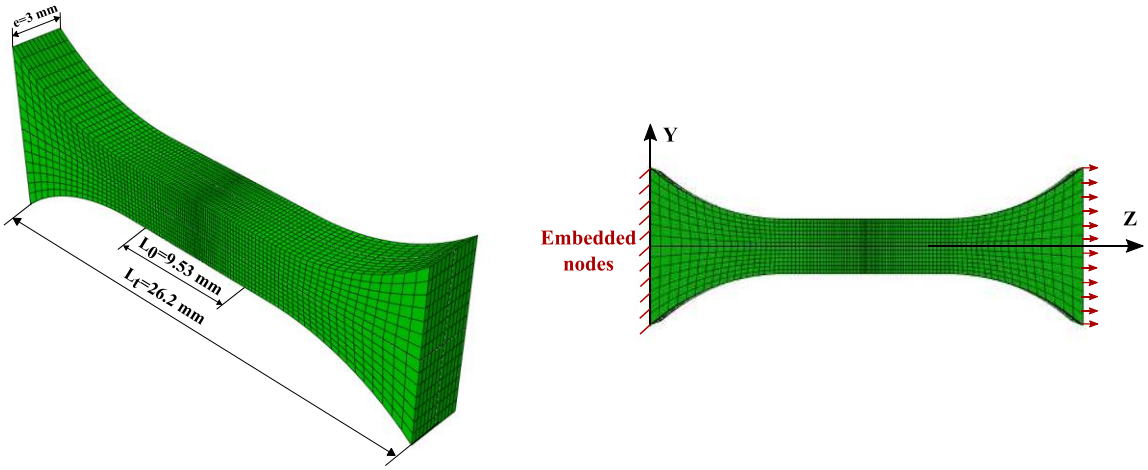

(a) (b)

Fig. 8. Numerical model: (a) geometrical information; (b) boundary conditions applied.

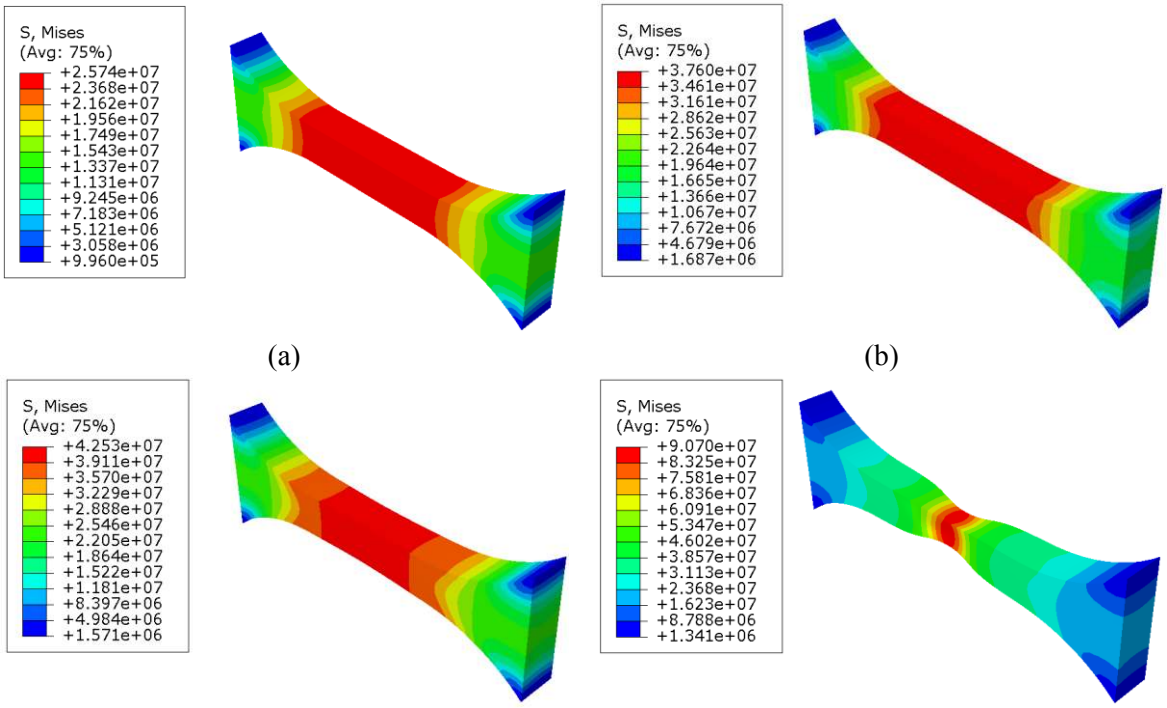

Fig. 9. Stress distribution at $\dot{\varepsilon}_0 = 0.1\ s^{-1}$ for: (a) UHMWPE at $\varepsilon = 0.2$ (b) UHMWPE at $\varepsilon = 0.5$ (c) HDPE at $\varepsilon = 0.2$ (d) HDPE at $\varepsilon = 0.5$.

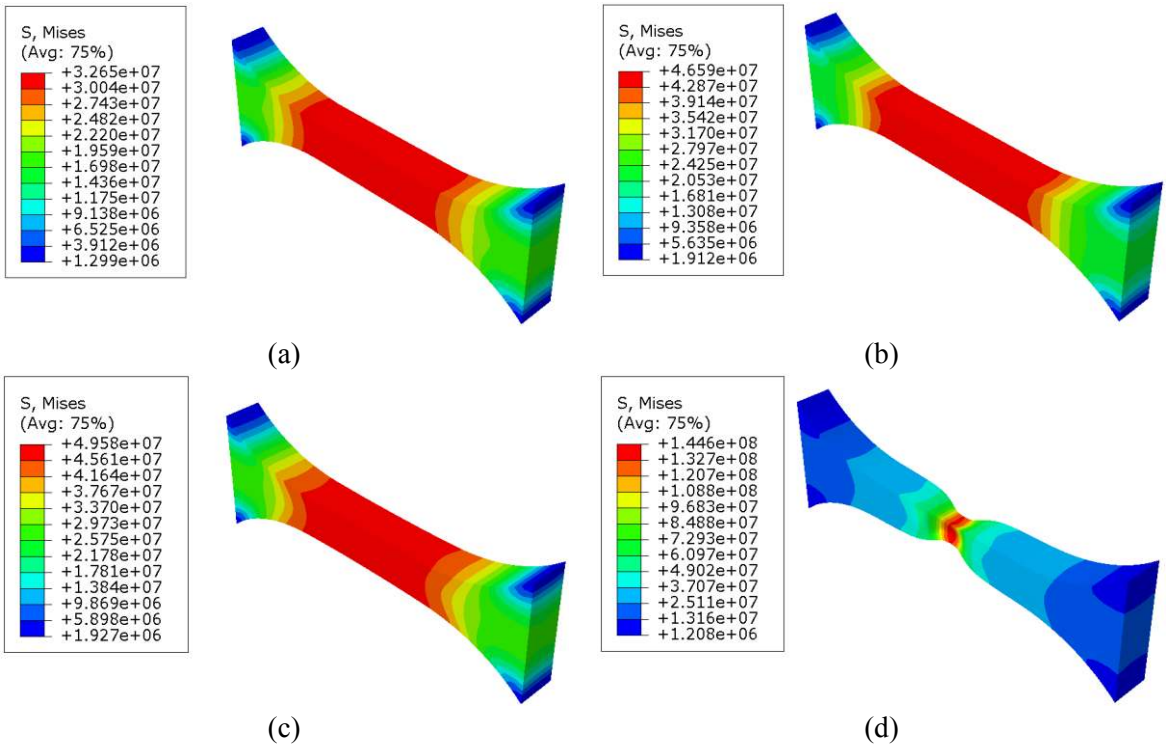

Fig. 10. Stress distribution at $\dot{\varepsilon}_0 = 100\ s^{-1}$ for: (a) UHMWPE at $\varepsilon = 0.2$ (b) UHMWPE at $\varepsilon = 0.5$ (c) HDPE at $\varepsilon = 0.2$ (d) HDPE at $\varepsilon = 0.5$.

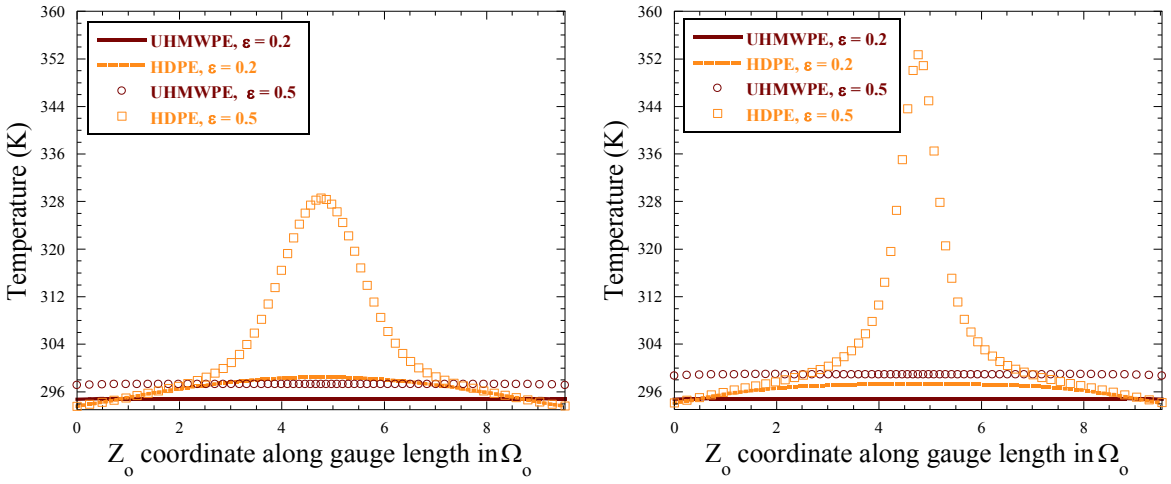

Fig. 11. Temperature distribution along gauge length at strains of 0.2 and 0.5 in UHMWPE and HDPE specimens at: (a) strain rate of 0.1 s^{-1}; and (b) strain rate of 100 s^{-1}.

Tables

Table 1
Material parameters for UHMWPE.

Initial elastic properties			**Intermolecular resistance**								
E_{ref} (GPa)	E_1 (MPa/K)	ν	$\dot{\varepsilon}_0$ (s^{-1})	C	σ_{T0} (MPa)	m	θ_{ref} (K)	θ_{melt} (K)	θ_{min} (K)	α	β
0.541	-6.5	0.46	0.1	0.048	37.5	0.7	293	406	198	1.0	1.0

Viscous resistance			**Network resistance**		
C_V (Pa)	$\bar{\lambda}_{VL}$	σ_{VT} (MPa)	C_R (MPa)	C_θ (MPa/K)	$\bar{\lambda}_L$
12.5	5	0.05	23	-0.15	5

General properties

ρ (kg/m^3)	Cp (J/Kg K)	α_θ (K^{-1})
940	1900	$124.5 \cdot 10^{-6}$

Table 2
Material parameters for HDPE.

Initial elastic properties			Intermolecular resistance								
E_{ref} (GPa)	E_1 (MPa/K)	ν	$\dot{\varepsilon}_0$ (s^{-1})	C	σ_{T0} (MPa)	m	θ_{ref} (K)	θ_{melt} (K)	θ_{min} (K)	α	β
0.782	-6.5	0.46	0.01	0.028	80	0.76	293	406	198	1.0	1.0

Viscous resistance			Network resistance		
C_V (Pa)	$\bar{\lambda}_{VL}$	σ_{VT} (Pa)	C_R (MPa)	C_θ (MPa/K)	$\bar{\lambda}_L$
(-)	(-)	(-)	12	-0.15	5

General properties		
ρ (kg/m^3)	Cp (J/Kg K)	α_θ (K^{-1})
970	1900	$93.6 \cdot 10^{-6}$

Appendix A. Nomenclature used in the formulation

Nomenclature			
$\{\Omega_o, \bar{\Omega}, \bar{\bar{\Omega}}, \tilde{\Omega}, \Omega\}$	initial, dilated, plastic dilated relaxed, viscous dilated relaxed and current configurations	$\bar{\bar{\mathbf{W}}}_{\mathbf{I}}^{\mathbf{p}}$	skew part of the plastic velocity gradient in Ω
$\bar{e}$	specific internal energy per unit volume in $\bar{\Omega}$	$\tilde{\mathbf{W}}_{\mathbf{V}}^{\mathbf{v}}$	skew part of the viscous velocity gradient in $\tilde{\Omega}$
$\bar{\mathbf{Q}}$	heat flux per unit volume in $\bar{\Omega}$	$\boldsymbol{\sigma}$	Cauchy stress tensor
$\bar{R}$	heat resource per unit volume in $\bar{\Omega}$	$\boldsymbol{\sigma}_{\mathbf{N}}$	network Cauchy stress tensor
$\bar{\eta}$	specific entropy per unit volume in $\bar{\Omega}$	$\boldsymbol{\sigma}_{\mathbf{I}}$	intermolecular Cauchy stress tensor
$\bar{C}$	heat capacity per unit volume in $\bar{\Omega}$	$\boldsymbol{\sigma}_{\mathbf{V}}$	viscous Cauchy stress tensor
$\{\theta, \theta_{ref}, \theta_{melt}, \theta_{min}\}$	current, reference, melting and lowest temperature considered	$\bar{\mathbf{S}}_{\mathbf{N}}$	network second Piola-Kirchhoff stress tensor in $\bar{\Omega}$
f_θ	temperature-dependent function	$\{\bar{\mathbf{S}}_{\mathbf{I}}, \bar{\bar{\mathbf{S}}}_{\mathbf{I}}\}$	intermolecular second Piola-Kirchhoff stress tensor in $\bar{\Omega}$ and $\bar{\bar{\Omega}}$
$\bar{\Psi}$	Helmholtz free energy per unit volume in $\bar{\Omega}$	$\bar{\mathbf{S}}_{\mathbf{V}}$	viscous second Piola-Kirchhoff stress tensor in $\bar{\Omega}$
$\bar{\nabla}_x$	gradient with respect to the point x in $\bar{\Omega}$	$\bar{\mathbf{M}}_{\mathbf{N}}$	network Mandel stress tensor in $\bar{\Omega}$
$\mathfrak{L}$	Langevin function	$\{\bar{\mathbf{M}}_{\mathbf{I}}, \bar{\bar{\mathbf{M}}}_{\mathbf{I}}\}$	intermolecular Mandel stress tensor in $\bar{\Omega}$ and $\bar{\bar{\Omega}}$
$\mathbf{I}$	Identity matrix	$\bar{\mathbf{M}}_{\mathbf{V}}$	viscous Mandel stress tensor in $\bar{\Omega}$
J_I	determinant of the intermolecular deformation gradient	$\bar{\lambda}$	average total stretch ratio
J_N	determinant of the network deformation gradient	$\bar{\lambda}_L$	locking stretch
J_V	determinant of the viscous deformation gradient	$\{I_{1I}, J_{2I}\}$	stress invariants of the intermolecular Mandel stress tensor
$\mathbf{F}$	deformation gradient	$\bar{\bar{\sigma}}_{eqI}$	Rhagava equivalent stress
$\mathbf{F}^{\boldsymbol{\theta}}$	thermal deformation gradient	g_I	plastic potential
$\mathbf{F}^{\mathbf{M}}$	mechanical deformation gradient	$\bar{\bar{\mathbf{r}}}_{\mathbf{I}}$	gradient of the plastic potential
$\mathbf{F}_{\mathbf{N}}^{\mathbf{e}}$	network elastic deformation gradient	$\dot{\bar{\bar{\gamma}}}_I^p$	viscoplastic multiplier
$\mathbf{F}_{\mathbf{I}}^{\mathbf{e}}$	intermolecular elastic deformation gradient	α_θ	thermal expansion coefficient
$\mathbf{F}_{\mathbf{I}}^{\mathbf{p}}$	intermolecular plastic deformation gradient	$\{\lambda_0, \mu_0\}$	classical Lamé constants
$\mathbf{F}_{\mathbf{V}}^{\mathbf{e}}$	viscoelastic elastic deformation gradient	E	Young's modulus
$\mathbf{F}_{\mathbf{V}}^{\mathbf{v}}$	viscoelastic viscous deformation gradient	$\{E_{ref}, E_1\}$	Young's modulus at the reference temperature and a specified material parameter
$\{\mathbf{C}_{\mathbf{N}}^{\mathbf{e}}, \mathbf{B}_{\mathbf{N}}^{\mathbf{e}}\}$	network elastic right and left Cauchy-Green tensor	$\{\sigma_T, \sigma_{T0}\}$	yield stress in uniaxial tension and its value at reference temperature
$\mathbf{C}_{\mathbf{I}}^{\mathbf{e}}$	intermolecular elastic right Cauchy-Green tensor	α	pressure sensitivity parameter
$\{\mathbf{C}_{\mathbf{V}}^{\mathbf{e}}, \mathbf{B}_{\mathbf{V}}^{\mathbf{e}}\}$	viscous elastic right Cauchy-Green tensor	β	volumetric plastic strain parameter
$\mathbf{l}$	velocity gradient	$\dot{\varepsilon}_0$	reference strain rate
$\mathbf{l}_{\mathbf{V}}^{\mathbf{e}}$	viscous elastic velocity spatial gradient	C	rate sensitivity parameter
$\bar{\mathbf{L}}^{\boldsymbol{\Theta}}$	thermal velocity gradient in $\bar{\Omega}$	m	temperature sensitivity parameter
$\tilde{\mathbf{L}}_{\mathbf{V}}^{\mathbf{v}}$	viscous velocity gradient in $\tilde{\Omega}$	C_R	initial elastic modulus of the network backstress resistance
$\bar{\bar{\mathbf{L}}}_{\mathbf{I}}^{\mathbf{p}}$	plastic velocity gradient in $\bar{\bar{\Omega}}$	C_θ	temperature-dependent material parameter controlling the elastic modulus of network
$\mathbf{d}_{\mathbf{N}}^{\mathbf{e}}$	symmetric part of the network elastic velocity gradient in Ω	C_v	initial elastic modulus of the viscous backstress resistance
$\mathbf{d}_{\mathbf{I}}^{\mathbf{e}}$	symmetric part of the intermolecular elastic velocity gradient in Ω	$\bar{\lambda}_V$	average viscous stretch ratio

$\mathbf{d_V^e}$	symmetric part of the viscous elastic velocity gradient in Ω	$\bar{\lambda}_{VL}$	viscous locking stretch
$\bar{\mathbf{D}}^{\mathbf{p}}$	symmetric part of the plastic velocity gradient in $\bar{\Omega}$	$\tilde{\mathbf{N}}_{\mathbf{V}}$	gradient of the viscoelastic flow
$\bar{\mathbf{D}}^{\boldsymbol{\nu}}$	symmetric part of the viscous velocity gradient in $\bar{\Omega}$	$\dot{\tilde{\gamma}}_V^{\nu}$	viscoelastic multiplier
$\bar{\bar{\mathbf{D}}}_{\mathbf{I}}^{\mathbf{p}}$	symmetric part of the intermolecular plastic velocity gradient in $\bar{\bar{\Omega}}$	τ_V	effective stress driving the viscous flow
$\tilde{\mathbf{D}}_{\mathbf{V}}^{\boldsymbol{\nu}}$	symmetric part of the intermolecular viscous velocity gradient in $\tilde{\Omega}$	σ_{VT}	Material parameter of the viscous resistance
$\bar{\mathbf{W}}^{\boldsymbol{\theta}}$	skew part of the thermal velocity gradient in $\bar{\Omega}$		